Petroleum Science 22 (2025) 1497–1512

Contents lists available at ScienceDirect

Petroleum Science

journal homepage: www.keaipublishing.com/en/journals/petroleum-science

Original Paper

# Exact P-wave reflection and transmission coefficients for horizontal transversely isotropic media at an imperfectly welded contact interface under in-situ horizontal stress

Xin-Peng Pan [a], [b], [c], Cheng-Xu Lu [d], [e], Hao-Wen Xu [b], [c], Da-Zhou Zhang [a], [b], [c], *

[a] Key Laboratory of Metallogenic Prediction of Nonferrous Metals and Geological Environment Monitoring (Central South University), Ministry of Education, Changsha, 410083, Hunan, China
[b] Hunan Key Laboratory of Nonferrous Resources and Geological Disaster Exploration, Central South University, Changsha, 410083, Hunan, China
[c] School of Geoscience and Info-Physics, Central South University, Changsha, 410083, Hunan, China
[d] State Key Laboratory of Deep Petroleum Intelligent Exploration and Development, Institute of Geology and Geophysics, Chinese Academy of Sciences, Beijing, 100029, China
[e] College of Earth and Planetary Sciences, University of Chinese Academy of Sciences, Beijing, 100049, China

ARTICLE INFO

*Article history:*
Received 9 April 2024
Received in revised form
28 September 2024
Accepted 12 February 2025
Available online 13 February 2025

Edited by Meng-Jiao Zhou and Teng Zhu

*Keywords:*
Exact *R*/*T* coefficients
Acoustoelasticity theory
Linear-slip theory
Stress-dependent parameters
Frequency-dependent formulations

ABSTRACT

A comprehensive understanding of exact seismic P-wave reflection and transmission (*R*/*T*) coefficients at imperfectly welded or non-welded contact interfaces holds paramount importance in the realm of seismic exploration. Nonetheless, scant attention has been devoted in previous literature to the investigation of stress-dependent exact *R*/*T* coefficients in horizontal transversely isotropic (HTI) media, characterized by a horizontal symmetry axis, at such interfaces. Addressing this scholarly gap, we present exact *R*/*T* coefficient formulations specifically tailored to an imperfectly welded contact interface separating two HTI media under the influence of in-situ horizontal stress. We begin by deriving the equation of motion for a stressed HTI medium, utilizing the theoretical framework of acoustoelasticity to examine the impact of in-situ horizontal stress on the overarching elastic properties of HTI media. Precise boundary conditions are then established at the imperfectly welded contact interface by applying generalized stress-strain relationships and linear-slip theory, with the influence of in-situ horizontal stress on the interface further explored through the linear-slip model. By integrating these elements with the seismic wave displacement equation, we derive exact *R*/*T* coefficient formulations applicable to an imperfectly welded contact interface between two HTI media. Numerical analyses are conducted to elucidate the effects of in-situ horizontal stress on critical parameters such as rock density, seismic wave velocity, Thomsen-type anisotropy parameters, *R*/*T* coefficients, and seismic reflection responses at the imperfectly welded contact interface. Furthermore, the proposed formulations are frequency-dependent, with the imperfectly welded contact interface acting as a frequency-selective filter for both reflected and transmitted waves. Notably, under conditions of sufficiently large incident angles, the sensitivity of *R*/*T* coefficients to key influencing factors increases significantly. The derived *R*/*T* coefficient formulations and the accompanying numerical results offer valuable insights for fracture characterization, stress-dependent parameter inversion, and in-situ stress detection.

## 1. Introduction

Formulations of seismic wave reflection and transmission (*R*/*T*) coefficients in transversely isotropic (HTI) media with a horizontal symmetry axis play a pivotal role in connecting observable seismic reflections to subsurface rock properties. These formulations are fundamental to seismic inversion processes, which are essential for fracture characterization and fluid identification, and thereby aid in enhancing the understanding of subsurface hydrocarbon reservoirs (Zong et al., 2013; Yin et al., 2015; Pan et al., 2018, 2020; Pan and Zhang, 2019). Extensive research has focused on parameterizing

---

* Corresponding author.
*E-mail address:* dazhou2005@163.com (D.-Z. Zhang).

https://doi.org/10.1016/j.petsci.2025.02.005

seismic $R/T$ characteristics, as demonstrated by seminal studies such as Rüger (1997), Chaisri and Krebes (2000), and Malehmir and Schmitt (2017). However, the explicit incorporation of in-situ stress, particularly horizontal principal stress, into the exact $R/T$ coefficients at imperfectly welded interfaces in weakly anisotropic HTI media has been inadequately addressed in existing literature.

The theory of acoustoelasticity, which describes the relationship between stress and wave propagation in elastic media, has long been used to explore the mechanical effects of in-situ stress on seismic wave behavior (Hughes and Kelly, 1953). Numerous studies have applied this theory to investigate seismic wave propagation in prestressed rock formations (Pao, 1984; Norris, 1995; Winkler et al., 1998; Sinha et al., 2000; Abiza et al., 2012; Pan et al., 2024). This theory, which explains elastic nonlinearities induced by wave-induced dynamic deformations under small prestresses, finds extensive application in investigating the stress-dependent elastic properties of rocks in both laboratory (Johnson and Rasolofosaon, 1996; Winkler and Liu, 1996; Winkler et al., 1998; Winkler and McGowan, 2004), borehole (Sinha et al., 1995; Sinha and Kostek, 1996; Sinha et al., 2000; Sinha and Plona, 2001), and seismic investigations (Bakulin et al., 2003; Liu et al., 2007). It encompasses elastic nonlinearities induced by wave-induced limited dynamic deformations under small prestresses. Moreover, acoustoelasticity is particularly effective in explaining stress-induced nonlinearities in elastic properties, where the third-order elastic constants characterize the stress-dependent variations in acoustic velocities across different wave modes (Sarkar et al., 2003; Prioul et al., 2004; Pan et al., 2024). This theoretical framework is fundamental to deriving $R/T$ coefficient formulations for interfaces subject to stress conditions.

Further, scholars have extensively explored additional factors affecting seismic responses, such as fluid-porous properties and geothermal field effects. Biot theory (Biot, 1956a, 1956b) first predicted velocity dispersion and amplitude attenuation in fluid-saturated porous media, giving rise to advanced poroelastic models that describe frequency dispersion, attenuation, and frequency-dependent anisotropic characteristics of seismic waves in such media (Yang and Zhang, 2000, 2002; Chapman, 2009; Yang et al., 2014; Carcione, 2015; Cheng, 2016; Zhang et al., 2019). Numerous models have also been developed to examine how pressure and frequency affect the elastic modulus and frequency-dependent azimuthal reflections of fluid-saturated rocks (Guo et al., 2015; Guo and Li, 2017; Sun and Gurevich, 2020; Fu et al., 2020; Chen et al., 2023a; Li et al., 2024). Acoustoelastic theory has been further extended to porous media, where it has been combined with anisotropic theory to derive seismic wave equations accounting for initial stress, exploring wave dispersion and attenuation in stressed porous media (Ba et al., 2013; Liu et al., 2021; Chen et al., 2023b). Additionally, the influence of geothermal effects on seismic wave propagation has been widely studied. Using acoustoelastic theory, scholars have investigated how seismic wave propagation and the coupled effects of stress and thermal fields influence rock elasticity (Hou et al., 2021; Chen et al., 2022a).

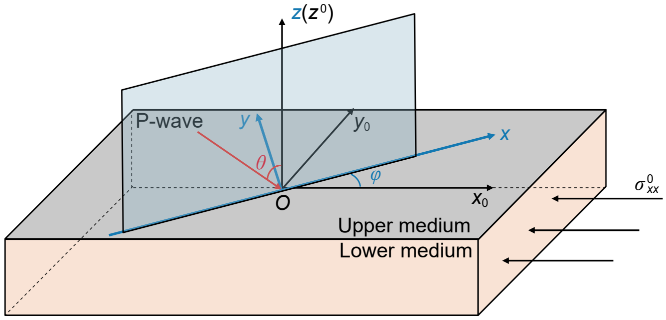

**Fig. 1.** Schematic diagram of a P-wave incident on a stressed HTI medium.

Early exploration of wave $R/T$ coefficients concentrated on interfaces between distinct elastic media, such as the classical Zoeppritz (1919) equation for isotropic media and its linear approximations (Aki and Richards, 1980). Over time, extensions were made to include anisotropic media (Rüger, 1997; Pšenčik &Vavryčuk, 1998; Pšenčik and Martins, 2001; Malehmir and Schmitt, 2017; Lu et al., 2018; Li et al., 2018) and viscoelastic media (Stovas and Ursin, 2003; Innanen, 2011). Yet, the incorporation of in-situ stress effects, particularly in anisotropic media, remains limited. Degtyar and Rokhlin (1998) were among the first to investigate the impact of stress on elastic wave propagation at interfaces between anisotropic media, while Liu et al. (2009) established a direct relationship between horizontal uniaxial stress and P-wave reflection coefficients in HTI media based on weak-anisotropy assumption (Thomsen, 1986; Rüger, 1997). Liu et al. (2016) further extended this work by deriving approximate S-wave reflection coefficients for interfaces involving isotropic and anisotropic stressed media. Chen et al. (2021) made significant advancements by deriving exact seismic $R/T$ coefficient equations of P and SV waves at welded interfaces between stressed media based on acoustoelasticity. Pan et al. (2023) also contributed by formulating approximate P-wave reflection coefficients for weakly anisotropic HTI media under horizontal in-situ stress. These studies underscore the importance of incorporating stress effects, yet they do not fully account for the complexities of imperfectly welded interfaces, such as fractures, joints, and faults, that are commonly encountered in natural reservoirs (Chaisri and Krebes, 2000; Cui et al., 2017; Chen et al., 2023a).

Imperfectly welded interfaces are often modeled using the linear-slip theory (Schoenberg, 1980; Pyrak-Nolte et al., 1990), which explains the discontinuity in displacement across a weakness plane, while stress continuity is maintained. This theory has been employed to derive analytical $R/T$ coefficient formulas for imperfectly welded interfaces, providing insights into seismic responses in fractured reservoirs (Schoenberg and Douma, 1988; Schoenberg and Protázio, 1990; Chaisri and Krebes, 2000; Cui et al., 2017). However, the impact of in-situ stress on R/T characteristics at such interfaces remains insufficiently explored. Recent studies have started to bridge this gap. Chen et al. (2022b) derived exact P-wave $R/T$ coefficients for imperfectly welded interface between two elastic isotropic half-spaces under vertical stress. Despite these advancements, the scarcity of exact $R/T$ formulations that consider in-situ horizontal stress at imperfectly welded interfaces in HTI media presents a significant obstacle to fully understanding stress-dependent seismic responses.

This study aims to address this gap by presenting exact $R/T$ coefficient formulations for seismic waves at an imperfectly welded interface between two HTI media under in-situ horizontal stress. Using acoustoelasticity theory and linear-slip boundary conditions, we first establish the boundary conditions for imperfectly welded interfaces. We then derive the motion equation for HTI media under horizontal stress, incorporating the effects of stress on elastic properties such as density, seismic wave velocity, and anisotropy parameters. By combining these elements, we formulate exact $R/T$ coefficients for HTI media at imperfectly welded interfaces. Numerical analysis explores how factors such as stress, incident angle, azimuth angle, and frequency influence seismic responses. Finally, we discuss the limitations of the method and suggest potential directions for future research.

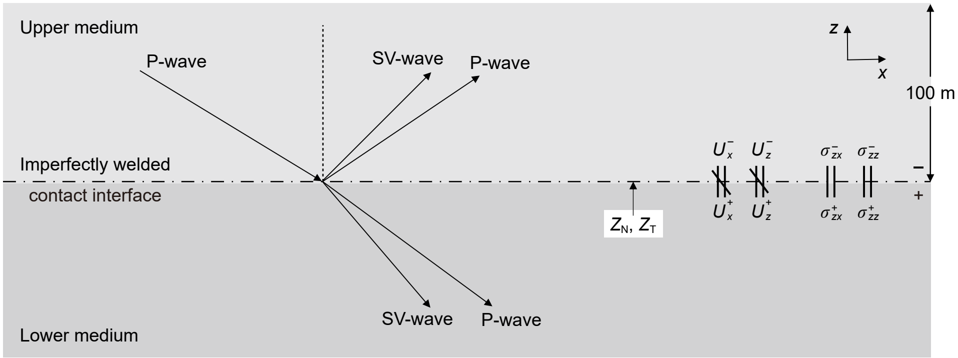

**Fig. 2.** Schematic diagram of seismic P-wave reflection and transmission at the imperfectly welded contact interface of stress layer (modified from Cui et al., 2017).

**Table 1**
Elastic properties of unstressed medium samples (Winkler and McGowan, 2004).

| Elastic properties | Saturated Castlegate sandstone | Saturated Portland sandstone | Dry Berea1 sandstone |
|---|---|---|---|
| $K$, GPa | 3.67 | 16.49 | 3.07 |
| $\lambda$, GPa | 1.50 | 11.86 | 0.321 |
| $\mu$, GPa | 3.25 | 6.94 | 4.13 |
| $\rho$, g/cm$^3$ | 2.00 | 2.33 | 2.04 |
| $V_{\mathrm{P0}}$, km/s | 2.00 | 3.32 | 2.05 |
| $V_{\mathrm{S0}}$, km/s | 1.27 | 1.73 | 1.42 |
| $A$, GPa | −1362 | −6559 | −5011 |
| $B$, GPa | −162.5 | −11751 | −1692 |
| $C$, GPa | −68 | −9377 | −158 |

## 2. Theory and method

### 2.1. Governing equations

The theory of acoustoelasticity is widely utilized to investigate the mechanical properties of prestressed elastic rocks. This framework provides a robust approach for modeling the stress-dependent behavior of rocks, independent of their geometric configurations or microstructural characteristics. Subsurface rocks typically exhibit three distinct states (Huang et al., 2001): 1) a natural state, free from any initial stress or strain; 2) an initial stressed state resulting from subsurface deformation or stress; and 3) a final state where seismic wave motion is superimposed upon the initial stress state.

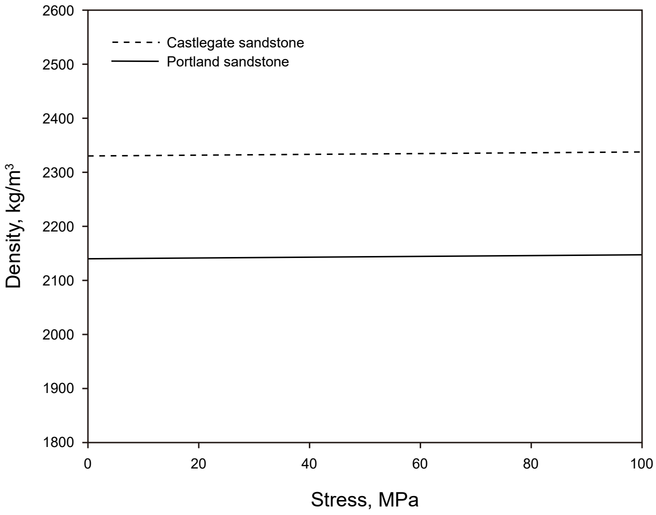

**Fig. 3.** Variation curves of density of two media under the in-situ horizontal stress.

As the rock particles transition from the natural state to the initial state, the displacement vector is denoted by $\mathbf{U}^0$. Similarly, the displacement from the natural state to the final state is represented by the vector $\mathbf{U}^{\mathrm{f}}$. The acoustoelastic equation for a stressed HTI medium, as formulated by Pao (1984), can be expressed as follows:

$$H_{\alpha\beta\gamma\delta}U_{\gamma,\beta\delta} = \rho\ddot{U}_{\alpha}. \tag{1}$$

where $H_{\alpha\beta\gamma\delta}$ denotes the acoustoelastic stiffness tensor. Cartesian tensor notation is employed in Eq. (1), in which the comma symbol denotes differentiation with respect to the subsequent component. For example, the notation $U_{\alpha}$ represents a component of the displacement vector from the transition between the initial state and the final state induced by seismic wave perturbation, the notation $U_{\gamma,\beta\delta}$ refers to a second partial derivative of the displacement component $U_{\gamma}$ with respect to the corresponding coordinate axis, and the notation $\ddot{U}_{\alpha}$ refers to the second derivative of $U_{\alpha}$ with respect to time. $\rho = \rho_0/(1+e_{\eta\eta}^0)$ signifies the density of the HTI media under stress, and $e_{\eta\eta}^0$ denotes the summation of principal strain induced by initial stress, with the subscripts indicating the directional components, as illustrated in Fig. 1. Unless otherwise specified, a corner mark beneath repeated tensors denotes summation. Here $e_{xx}^0$, $e_{yy}^0$ and $e_{zz}^0$ represent the initial strain components generated by the medium in the direction of the three axes under in-situ initial stress, respectively.

Additionally, the acoustoelastic stiffness tensor $H_{\alpha\beta\gamma\delta}$ in Eq. (1) can be expressed as

$$H_{\alpha\beta\gamma\delta} = C_{\alpha\beta\gamma\delta} + \sigma_{\beta\delta}^0\delta_{\alpha\gamma}, \tag{2}$$

where $C_{\alpha\beta\gamma\delta}$ represents the effective elastic stiffness tensor, and $\delta_{\alpha\gamma}$ represents the Kronecker delta. Consequently, we can derive the

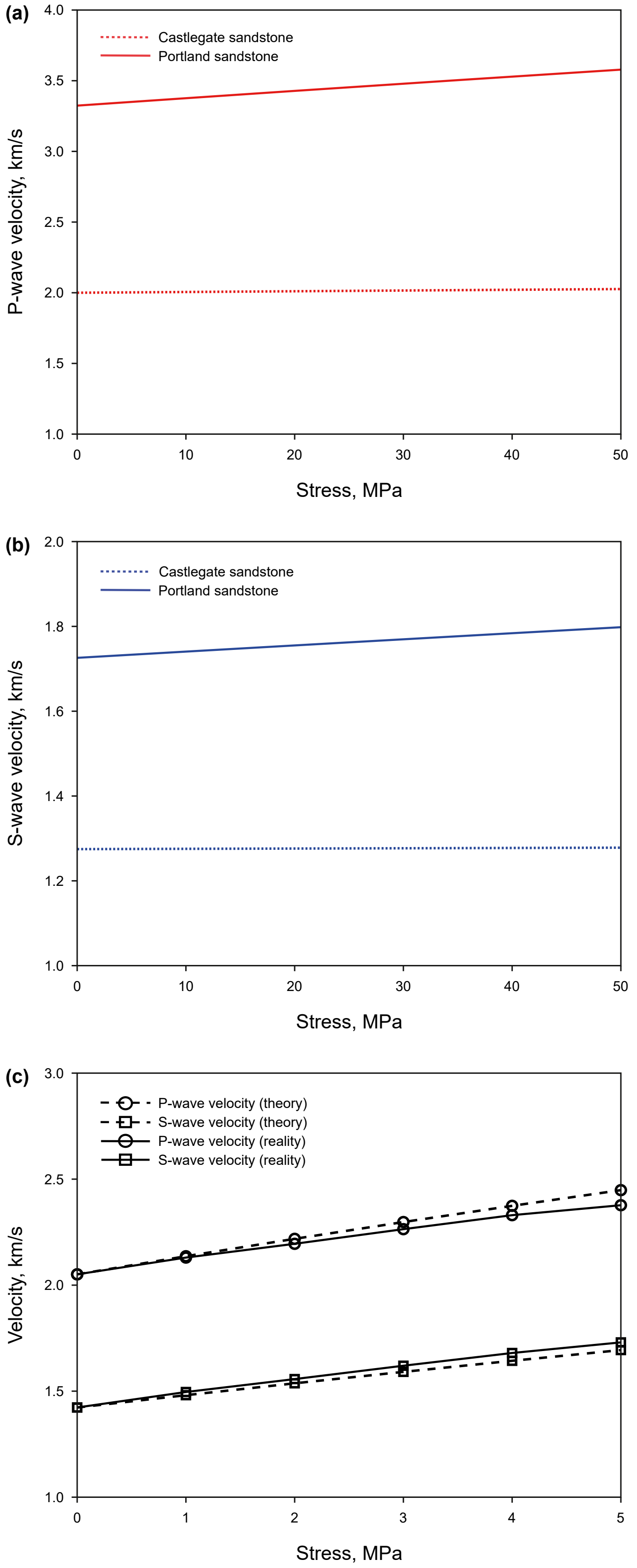

**Fig. 4.** Variation curves of vertical wave velocity of three media under the in-situ horizontal stress.

vertical wave velocity (Thomsen, 1986) and anisotropic parameters (Rüger, 1997; Tsvankin, 1997) of HTI media using the acoustoelastic stiffness tensor $H_{\alpha\beta\gamma\delta}$. For more information regarding the acoustoelastic stiffness tensor and additional details, please refer to Appendix A.

### 2.2. Time-harmonic wave solution in stressed HTI media

When HTI media are subjected to in-situ horizontal stress, as illustrated in Fig. 1, $\theta$ represents the incident angle, defined as the angle between the $z$-axis and the incident P-wave propagating in the $x$-$z$ plane. Additionally, $\varphi$ represents the azimuth angle, which represents the angle between the incident plane and the symmetry plane. A time-harmonic wave is employed to describe the displacement vector in Eq. (1):

$$U_\gamma(X,t) = A_\gamma \exp[jk(n_\alpha X_\alpha - Vt)], \tag{3}$$

where $A_\gamma = AP_\gamma$ is the component of the amplitude vector, with $A$ representing its modulus and $P_\gamma$ as the component of polarization vector. $n_\alpha$ denotes the component of propagation direction vectors, $X_\alpha$ represents the coordinate axis with $\alpha = x, y, z$. $V = \omega/k$ represents the phase velocity of waves, with $\omega$ representing the angular frequency and $k$ as the wavenumber, and $t$ represents the propagation time. Substituting Eq. (3) into Eq. (1) yields

$$\left(H_{\alpha\beta\gamma\delta} n_\alpha n_\delta - \rho V^2 \delta_{\beta\gamma}\right) P_\gamma = 0. \tag{4}$$

The polarization component $P_\gamma$ and phase velocity $V$ of the medium are determined by solving Eq. (4). It is important to note that the polarization direction exhibits a non-zero value, leading to non-trivial solutions:

$$\left| H_{\alpha\beta\gamma\delta} n_\alpha n_\delta - \rho V^2 \delta_{\beta\delta} \right| = 0. \tag{5}$$

By substituting the wave direction vector into Eq. (4), the corresponding phase velocities can be derived. These phase velocities will be employed in the subsequent derivation of the governing equations.

### 2.3. P-wave R/T coefficient formulas at an imperfectly welded contact interface

When a P-wave encounters an imperfectly welded contact interface between two layers in the $x$-$z$ plane, shear wave splitting or birefringence does not occur. In this case, only four types of reflected and transmitted waves are generated: the reflected P-wave, reflected SV-wave, transmitted P-wave, and transmitted SV-wave. The SH wave, which typically propagates along the surface, is absent in this scenario, and therefore does not require further discussion, as depicted in Fig. 2. This absence simplifies the wave interaction analysis at the interface, allowing us to focus solely on the reflected and transmitted P- and SV-wave modes, which are critical for understanding the energy partitioning across the interface in anisotropic media. In addition, the black arrows indicate the directions of wave propagation. The dashed line between the upper and lower media signifies the imperfect welded contact interface. The parameters $Z_\mathrm{T}$ and $Z_\mathrm{N}$ (Worthington and Lubbe, 2007) denote the tangential and normal fracture compliances, respectively. Slashes between parameters $U^+$ and $U^-$ represent the discontinuity in the displacement vector at the interface, while

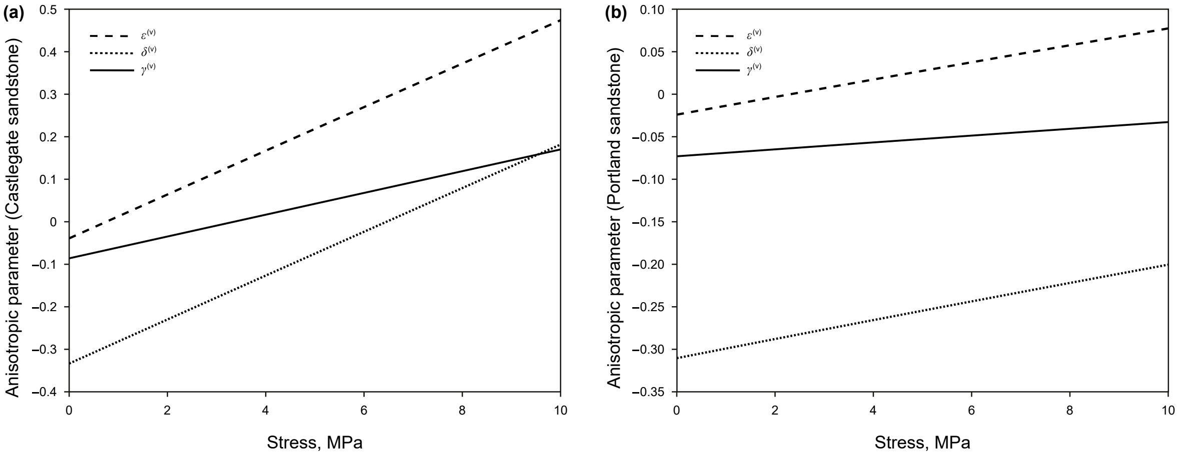

**Fig. 5.** Diagram of anisotropic parameters $\varepsilon^{(v)}$, $\delta^{(v)}$, $\gamma^{(v)}$ of **(a)** Castlegate sandstone and **(b)** Portland sandstone varying under the in-situ horizontal stress.

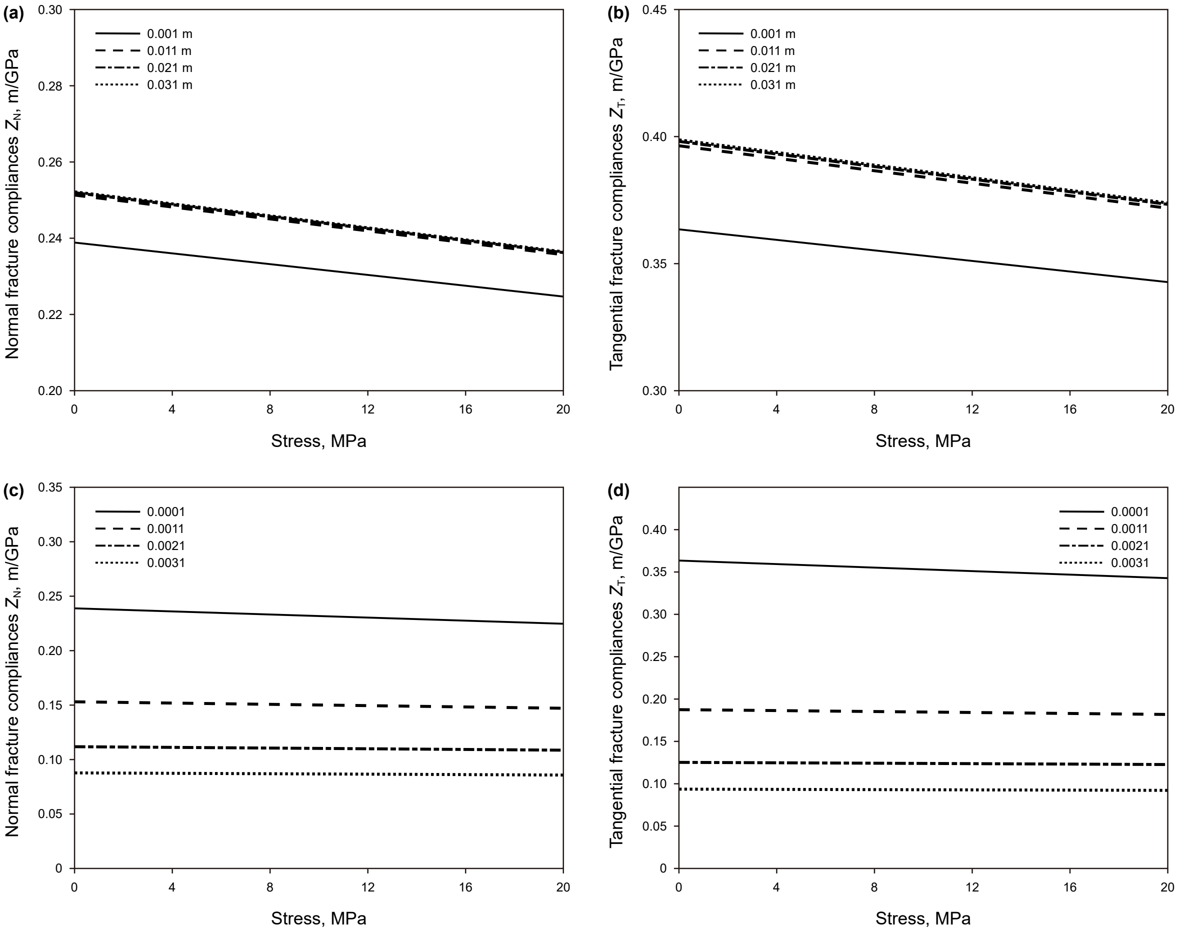

**Fig. 6.** Diagram of $Z_T$ and $Z_N$ varying with in-situ horizontal stress, in which **(a)** and **(b)** fixed $r^w$ to 0.0001 and change $d$, while **(c)** and **(d)** fixed $d$ to 0.001m and change $r^w$.

their absence between parameters $\sigma^+$ and $\sigma^-$ represent the continuity of the stress vector.

According to the linear-slip theory proposed by Schoenberg (1980), the boundary conditions governing an imperfectly welded contact interface dictate that the traction force remains continuous across the interface, whereas the displacement experiences a discontinuity proportional to the traction. These boundary conditions can be expressed as follows:

$$\Delta U_i = \Pi_{ii}\cdot\sigma_{zi}, i = x, z, \tag{6}$$

$$\sigma_{zi}^{+} = \sigma_{zi}^{-}, i = x, z, \tag{7}$$

where the superscripts + and − represent the upper and lower media, respectively. Here $\Delta U = U_i^+ - U_i^-$ $(i = x, z)$ represents the discontinuity in the displacement vector at the interface, and $\sigma_{zi}$

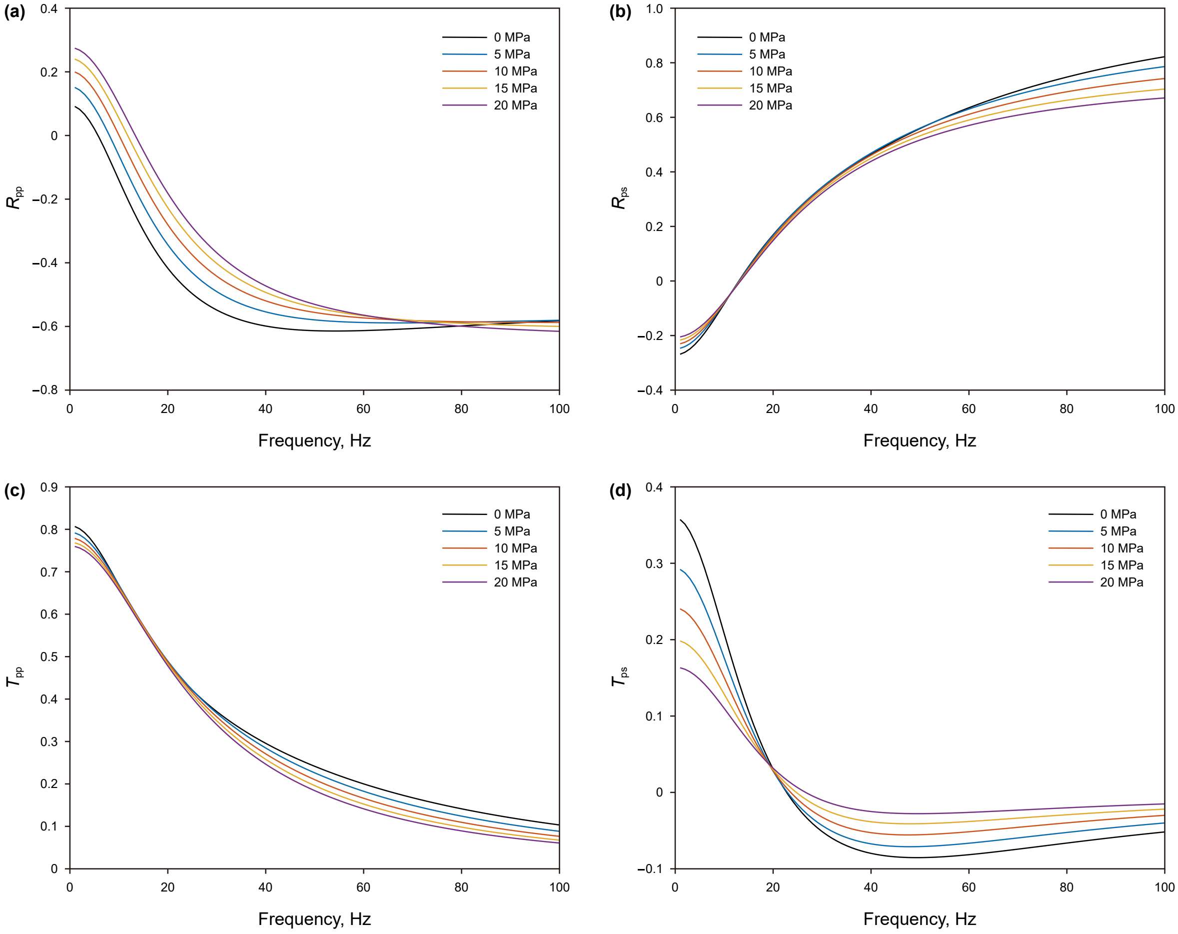

**Fig. 7.** Diagram of $R/T$ coefficients varying with in-situ horizontal stress and frequency **(a)** $R_{pp}$ **(b)** $R_{ps}$ **(c)** $T_{pp}$ **(d)** $T_{ps}$ (Incident angle is 30°, azimuth angle is 0°).

denotes the total stress tensor at the interface. Additionally, $\mathbf{\Pi}$ denotes the fracture compliance matrix, mathematically represented as

$$\mathbf{\Pi} = \begin{pmatrix} Z_T & 0 & 0 \\ 0 & 0 & 0 \\ 0 & 0 & Z_N \end{pmatrix}. \tag{8}$$

These parameters are key in characterizing the discontinuity at an imperfectly welded contact interface. Under applied stress, such an interface can undergo compression, leading to stress dependencies for both $Z_T$ and $Z_N$. These dependencies are relevant to the stress-dependent $R/T$ responses at the interface. If an imperfectly welded contact interface is characterized by a random distribution of circular contact points (e.g. fractures, faults, or joints), the fracture compliances $Z_T$ and $Z_N$ can be computed using the intrinsic fracture parameters and background elastic parameters. This provides the basis for studying the stress-dependent characteristics of such interfaces. Further details are provided in Appendix B.

The acoustoelastic constitutive relationship under in-situ horizontal stress, as formulated by Degtyar and Rokhlin (1998), can be expressed as

$$\sigma_{\alpha\beta} = H_{\alpha\beta\gamma\delta} e_{\gamma\delta} + U_{\alpha,\gamma} \sigma^0_{\gamma\beta}, \tag{9}$$

where $e_{\gamma\delta}$ represents the total strain tensor resulting from wave disturbance.

By combining the boundary conditions expressed by Eqs. (6) and (7) with Eq. (9), the exact $R/T$ coefficient formulas for stressed HTI media at an imperfectly welded contact interface are derived as

$$\mathbf{\Gamma}\mathbf{\Lambda} = \mathbf{M}. \tag{10}$$

The elements in Eq. (10) are detailed in Appendix C. This equation encapsulates the primary findings of this study, describing how in-situ horizontal stress influences the $R/T$ coefficients of waves at an imperfectly welded contact interface in HTI media. These coefficients account for factors such as in-situ horizontal stress, frequency, incident angle, and azimuth angle, providing insights into the fluctuations of the $R/T$ coefficients. Furthermore, the derived $R/T$ coefficients can be applicable in seismic forward modeling. It is important to note that, during the derivation, equal magnitudes of in-situ horizontal stress were assumed for the two media.

## 3. Numerical analysis

We employ two media types, namely Castlegate sandstone and Portland sandstone, to represent the objects under study, as illustrated in Table 1 (Winkler and McGowan, 2004). To address the impact of various factors on the $R/T$ coefficients, we specify the properties of the two media, and $A$, $B$ and $C$ (Goldberg, 1961) represent the third-order elastic constants, which depends on the type of rock. Specifically, our model involves saturated Castlegate sandstone for the upper medium and saturated Portland sandstone

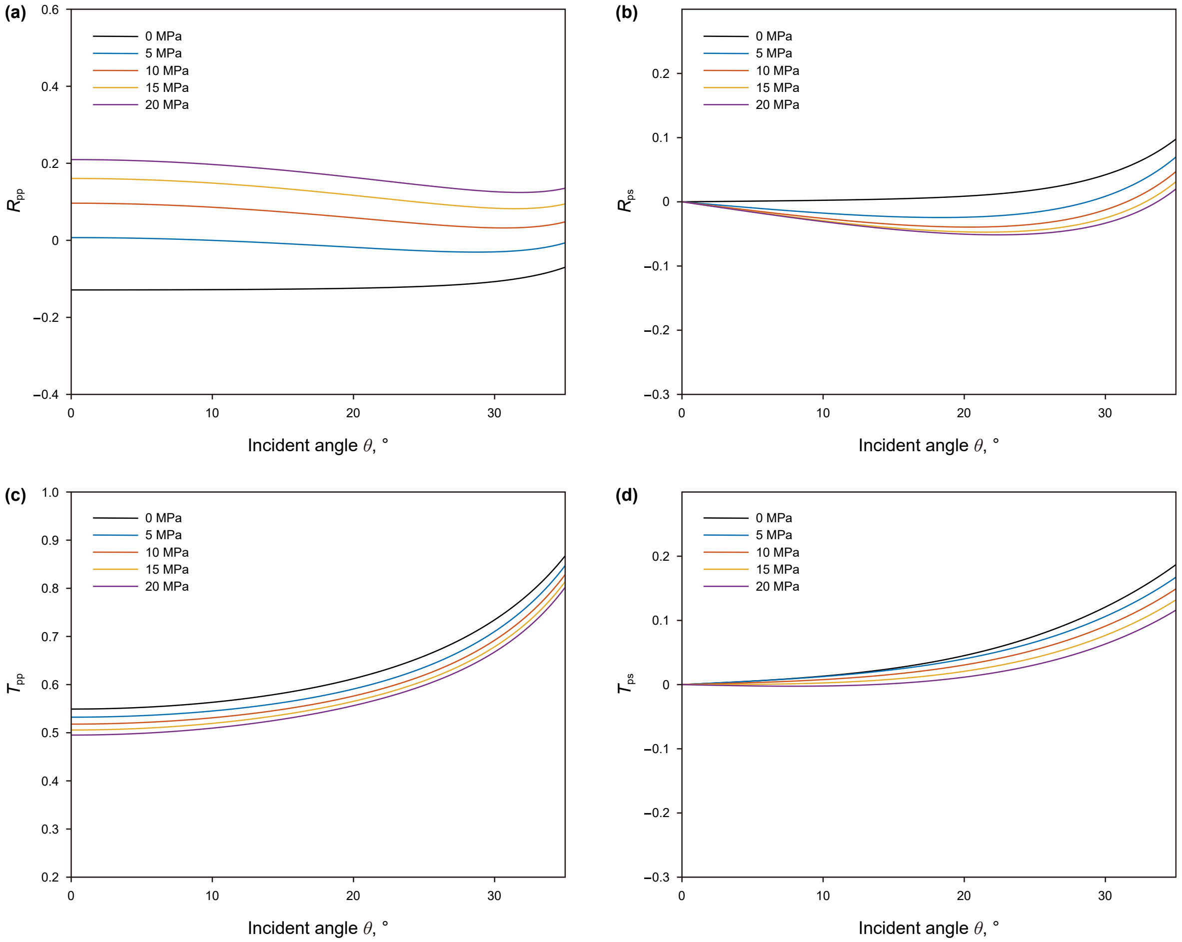

**Fig. 8.** Diagram of $R/T$ coefficients varying with in-situ horizontal stress and incident angle **(a)** $R_{pp}$ **(b)** $R_{ps}$ **(c)** $T_{pp}$ **(d)** $T_{ps}$ (The frequency is 10 Hz, and the azimuth angle is 0°).

for the lower medium.

Moreover, we utilize ideal anisotropic parameter values for Castlegate sandstone ($\varepsilon_1^{(\mathrm{v})} = -0.039$; $\delta_1^{(\mathrm{v})} = -0.054$; $\gamma_1^{(\mathrm{v})} = -0.086$) and Portland sandstone ($\varepsilon_2^{(\mathrm{v})} = -0.024$; $\delta_2^{(\mathrm{v})} = -0.091$; $\gamma_2^{(\mathrm{v})} = -0.073$) to investigate the impact of stress on the anisotropic parameters of HTI media. Additionally, based on the linear-slip model, the stress dependence of $Z_\mathrm{T}$ and $Z_\mathrm{N}$ are ideally explained according to the influence of stress on fracture aperture, respectively. Subsequently, we designate the thickness of the upper layer as 100 m (as depicted in Fig. 2) to analyze the seismic reflection response and the resulting reflection coefficients in the model.

### 3.1. Effect of stress on density, wave velocity and elastic anisotropy

The elastic properties, including density, wave velocity and elastic anisotropy of rock formations, undergo discernible changes when exposed to in-situ horizontal stress. Fig. 3 delineates the variations in density across the two media under stress conditions. Additionally, Figs. 4 and 5 depict the fluctuations in the vertical phase velocities of seismic waves propagation within the two media, as well as three Thomsen-type parameters ($\varepsilon^{(\mathrm{v})}$, $\delta^{(\mathrm{v})}$, and $\gamma^{(\mathrm{v})}$). These figures offer valuable insights into the modifications in rock properties and anisotropy arising from the influence of stress.

From Fig. 3, it is evident that as the stress magnitude varies from 0 to 100 MPa, there is minimal change in the density of both Castlegate sandstone and Portland sandstone, as indicated by $\rho = \rho_0/(1+e_{nn})$. This suggests that the influence exerted by stress is negligible. This outcome aligns with the experimental findings of Winkler and McGowan (2004), thereby validating the accuracy of our theoretical framework. Overall, the density of the rock exhibits minimal alteration under very low stress conditions.

Examining Fig. 4(a) and (b), we observe that with the stress magnitude ranging from 0 to 50 MPa, the vertical velocities of P and S waves for both rock types increase. This implies that both $H_{33}$ and $H_{44}$ are concurrently augmented. Moreover, the vertical velocity of Castlegate sandstone exhibits a more pronounced change compared to Portland sandstone, indicating that Castlegate sandstone is more sensitive to stress than Portland sandstone.

In addition, Berea1 sandstone from Table 1 is utilized to compare the measured rock wave velocity values from laboratory measurements with the theoretically predicted rock wave velocity, as shown in Fig. 4(c), which explores the variation in wave velocity of Berea1 sandstone under the influence of horizontal *in situ* stress, comparing it with laboratory data from Winkler and McGowan (2004). The results demonstrate a close match between theoretical calculations and laboratory measurements, affirming the accuracy of the acoustoelastic theoretical model.

In Fig. 5, it is evident that as the stress magnitude increases from 0 to 10 MPa, the anisotropic parameters of both Castlegate sandstone and Portland sandstone exhibit a linear change. Notably,

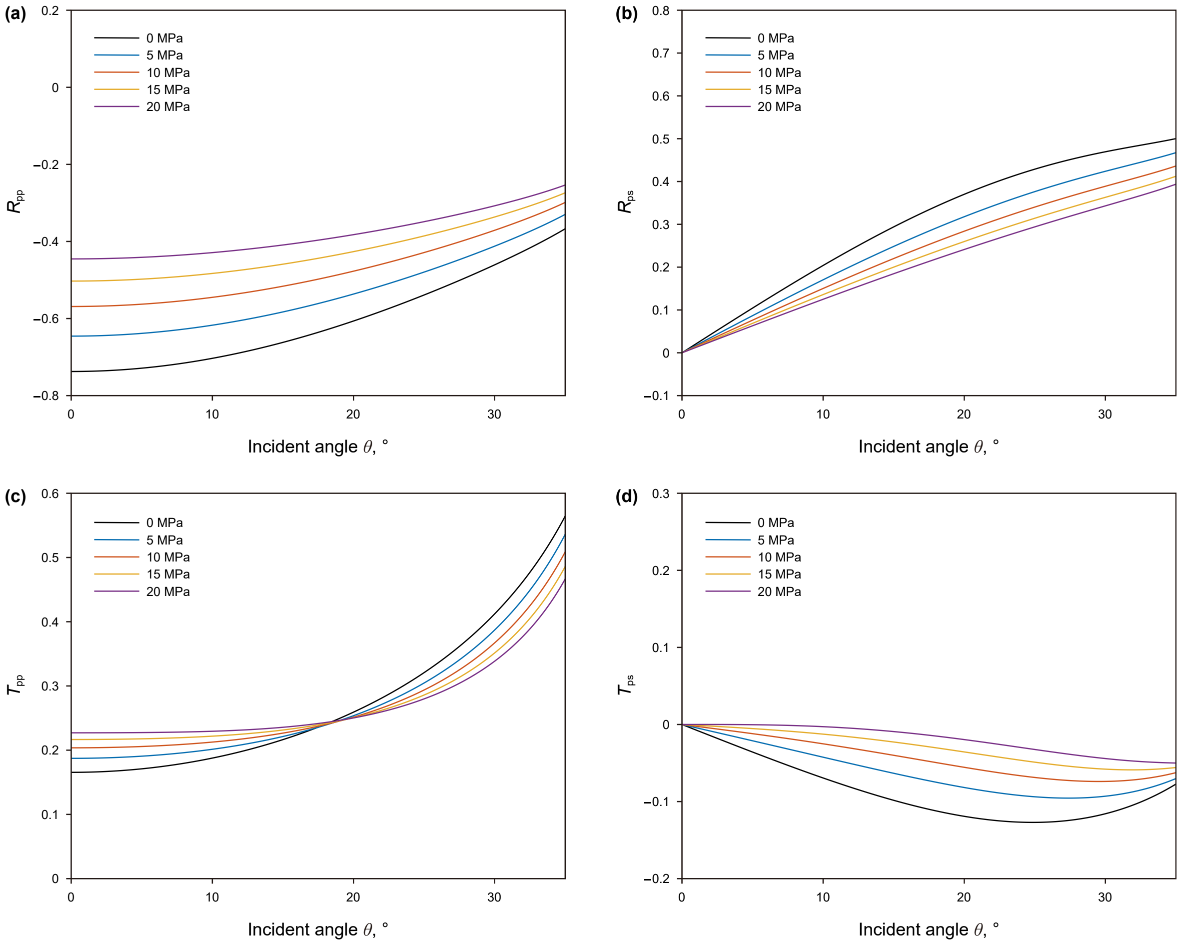

**Fig. 9.** Diagram of $R/T$ coefficients varying with in-situ horizontal stress and incident angle **(a)** $R_{pp}$ **(b)** $R_{ps}$ **(c)** $T_{pp}$ **(d)** $T_{ps}$ (The frequency is 30 Hz, and the azimuth angle is 0°).

Castlegate sandstone displays a higher sensitivity to in-situ horizontal stress compared to Portland sandstone, a trend consistent with the observed changes in vertical velocity. Despite differences in the initial idealized values and the nature of the medium employed, the variation trends of the three anisotropic parameters remain similar. This not only elucidates the impact of stress on the media's anisotropy but also reaffirms the robustness and consistency of the theoretical framework.

### 3.2. Effect of stress on imperfectly welded contact interface

This section studies the stress dependences of $Z_T$ and $Z_N$, which can be used to characterize the imperfectly welded contact interface. We suppose the imperfectly welded interface is filled with soft material, whose bulk moduli $K$ and shear moduli $\mu$ are 0.5 GPa and 2 GPa, respectively. The ratio of S-wave velocity to P-wave velocity of the Castlegate sandstone is approximately 0.635, and the initial average aperture $d$ of the imperfectly welded interface is 0.8 m. The shear modulus $\mu^*$ of Castlegate sandstone is 3.25 GPa.

Fig. 6 offers valuable insights into the influence of in-situ horizontal stress on $Z_T$ and $Z_N$. Fig. 6(a) and (b) represent the results with the ratio of welded contact to fracture area $r^w$ is fixed to 0.0001, and the average radius $d^*$ of the welded contact areas is changed to 0.001, 0.011, 0.021, and 0.031 m. Fig. 6(c) and (d) represent the results with the average radius $d^*$ of the welded contact areas is fixed to 0.001 m, and the ratio of welded contact to fracture area $r^w$ is changed to 0.0001, 0.0011, 0.0021, and 0.0031.

As depicted in Fig. 6, both $Z_T$ and $Z_N$ change linearly and are inversely proportional to the increasing in-situ horizontal stress. And the change of $r^w$ and $d^*$ can notably affect the magnitude of $Z_T$ and $Z_N$ with the opposite effect, but has little effect on their stress sensitivity. Moreover, the change of $Z_T$ and $Z_N$ becomes smaller with the increase of $r^w$ and $d^*$. The numerical simulation provides a simple insight into the influence of in-situ horizontal stress on imperfectly welded contact interface, and lays a foundation for the derived of the exact $R/T$ coefficient formulas for stressed HTI media at an imperfectly welded contact interface.

### 3.3. Effect of stress and frequency on R/T coefficients

Fig. 7 offers valuable insights into the influence of in-situ horizontal stress and frequency on the variation of $R/T$ coefficients, with an incident angle of 30° and an azimuth angle of 0°. The frequency ranges from 0 to 100 Hz, while the stress level varies across five values from 0 to 20 MPa. These visualizations provide a comprehensive depiction of the trends in R/T coefficients concerning in-situ horizontal stress and frequency, thereby enhancing our understanding of their fluctuations.

As depicted in Fig. 7, both $R_{pp}$ and $T_{ps}$ exhibit a direct proportionality to frequency, whereas $R_{ps}$ demonstrates an inverse proportionality to frequency. Moreover, $T_{pp}$ initially decreases within the frequency range of 0–40 Hz, but exhibits an increase at frequencies surpassing 40 Hz. These findings underscore the function of the imperfectly welded contact interface as a pass filter for both

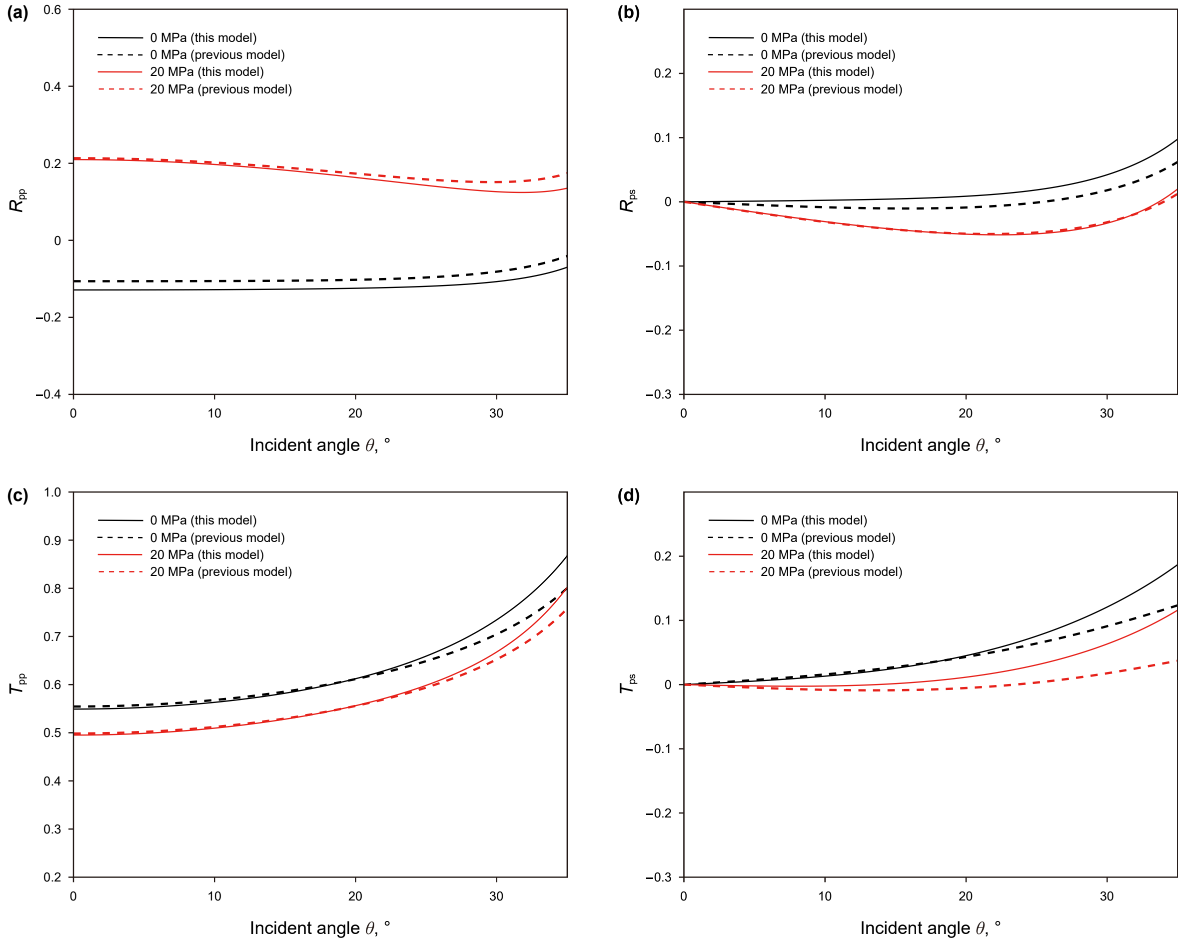

**Fig. 10.** Comparison diagram of $R/T$ coefficients in two models varying with in-situ horizontal stress and azimuth angle **(a)** $R_{pp}$ **(b)** $R_{ps}$ **(c)** $T_{pp}$ **(d)** $T_{ps}$ (The frequency is 10 Hz, and the azimuth angle is 0°).

reflected and transmitted waves. Furthermore, the observations highlight the varying sensitivity of $R/T$ coefficients to stress across different frequencies of seismic waves.

### 3.4. Effect of stress and incident angle on R/T coefficients

Figs. 8 and 9 depict the impact of in-situ horizontal stress and incident angle on the variation of $R/T$ coefficients, with Fig. 8 corresponding to a frequency of 10 Hz and Fig. 9 to a frequency of 30 Hz. The incident angle ranges from 0° to 35°, and while the stress levels are graded across five values from 0 to 20 MPa. These visual representations offer insights into the trends in $R/T$ coefficients concerning in-situ horizontal stress and incident angle, facilitating a clear observation of their fluctuations.

As depicted in Fig. 8, at a frequency is 10 Hz, both coefficients $R_{pp}$ and $T_{pp}$ exhibit a positive correlation with stress across the range of incident angles, while the correlation with incident angle for these two coefficients varies. Furthermore, it's noteworthy that the influence of stress varies across different incident angles. Additionally, upon observing Fig. 9, the general trend of $R/T$ coefficients mirrors that of Fig. 8. However, the sensitivity to stress markedly differs between the two cases due to the frequency variance.

As mentioned earlier, while a model for an imperfectly welded contact interface between two stressed isotropic media has been previously reported (Chen et al., 2022b), our study focuses on HTI media. By comparing the two models, we can discern the effect of anisotropic parameters on reflection amplitude or amplitude variation with offset (AVO) characteristics, as depicted in Fig. 10. The condition depicted in Fig. 10 is identical to those in Fig. 8. In Fig. 10, lines of different colors represent varying stress levels, with solid lines denoting the model presented in this study, and dotted lines representing the previously reported model. From Fig. 10, it is evident that the $R/T$ coefficients exhibit increased sensitivity to anisotropic parameters with rising incidence angles. Additionally, the sensitivity shifts with increases in in-situ horizontal stress, attributable to the presence of stress-induced anisotropy. Furthermore, while our model adopts the weak anisotropy hypothesis, real strata typically exhibit stronger anisotropy. Therefore, future studies will need to explore more practical physical mechanisms to refine our model.

### 3.5. Effect of stress and azimuth angle on R/T coefficients

Figs. 11 and 12 illustrate the impact of in-situ horizontal stress and azimuth angle on the variability of $R/T$ coefficients across two scenarios, where the incident angle is fixed at 30°. Fig. 11 corresponds to a frequency of 10 Hz, while Fig. 12 corresponds to a frequency of 30 Hz. The azimuth angle spans from 0° to 360°, while the stress levels encompass five values ranging from 0 to 20 MPa. These visualizations offer a detailed insight into the trends observed in $R/T$ coefficients concerning in-situ horizontal stress and

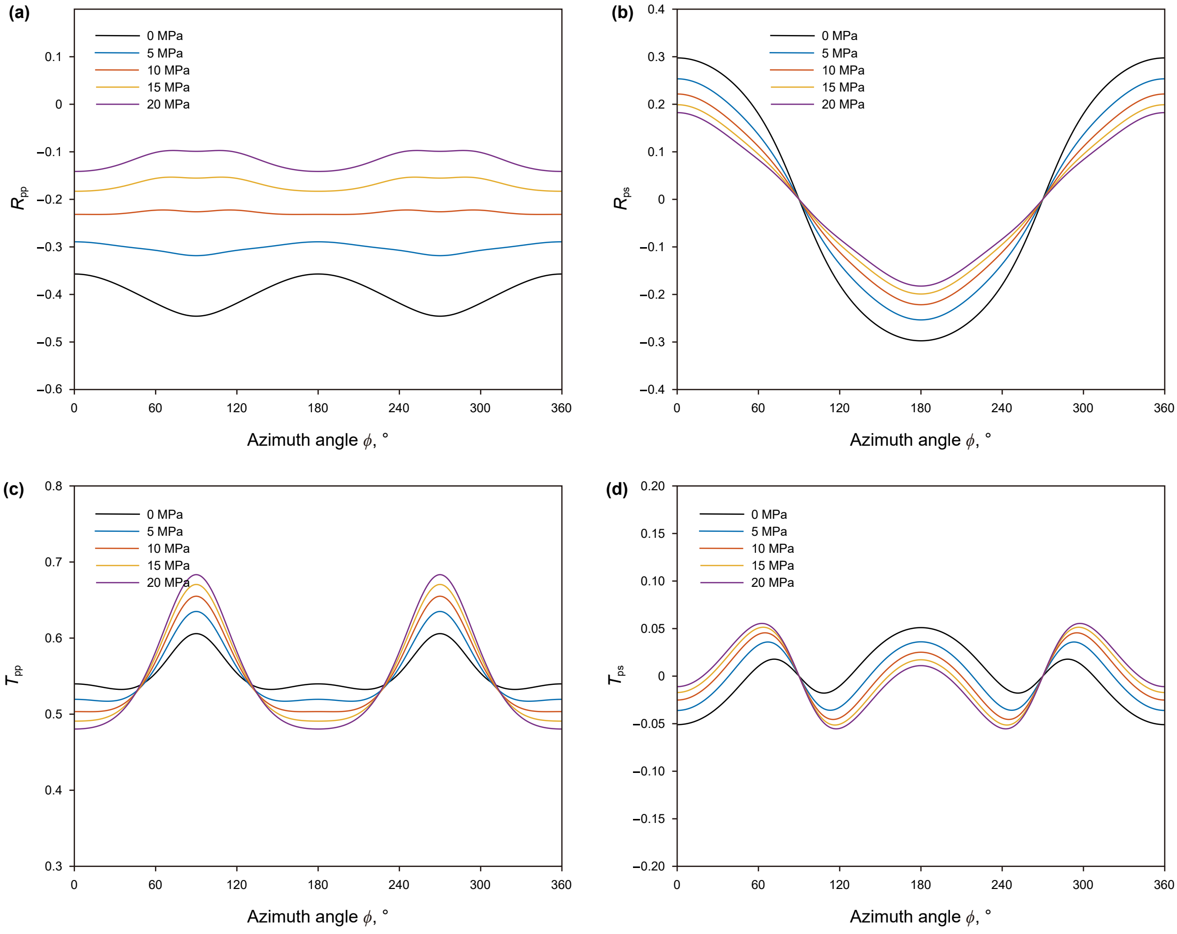

**Fig. 11.** Diagram of $R/T$ coefficients varying with in-situ horizontal stress and azimuth angle **(a)** $R_{\mathrm{pp}}$ **(b)** $R_{\mathrm{ps}}$ **(c)** $T_{\mathrm{pp}}$ **(d)** $T_{\mathrm{ps}}$ (The frequency is 10 Hz, and the incident angle is 30°).

azimuth angle, facilitating a comprehensive comprehension of their fluctuations.

The $R/T$ coefficients demonstrate periodic behavior across the azimuthal spectrum. Under the influence of simple stress on HTI media, this periodicity remains consistent. However, with more complex stress patterns, the periodicity may undergo alterations. Despite variations in frequency attributable to diverse initial conditions, the overarching trend in $R/T$ coefficient variation remains largely uniform between the two scenarios. The predictable response of $R/T$ coefficients to stress suggests the potential for reliably inferring or forecasting in-situ stress levels based on observed P-wave seismic signals through suitable physical methodologies.

### *3.6. Effect of stress, incident angle and frequency on R/T coefficients*

In real seismic field data, such as partial stacks, the seismic reflection amplitude is influenced by both incident angles and the frequency ranges of the seismic data (Yang et al., 2022). To accurately reflect this real-world scenario, we model the $R/T$ coefficients as a function of both incident angles and frequencies, as depicted in Fig. 13. Here, the incident angle ranges from 0° to 35°, while the frequency spans from 1 to 100 Hz. Additionally, the stress levels are set at 5 MPa, varying across five increments from 0 to 20 MPa. These visualizations serve as a fundamental basis for implementing forward modeling procedures that account for the frequency-angle dependence observed in actual geological formations under stress.

### *3.7. Effect of stress on 3D seismic response characteristics*

We then examine the collective influence of three factors and present three-dimensional representations illustrating the variation of $R/T$ coefficients with incident angle, azimuth angle, and in-situ horizontal stress for two specific scenarios. Fig. 14 corresponds to the case of 10 Hz, while Fig. 15 represents the case of 30 Hz. As depicted in Figs. 14 and 15, the incident angle ranges from 0° to 35°, the azimuth angle spans from 0° to 360°, and the stress levels are set at 5 MPa, varying across five increments from 0 to 20 MPa. These figures offer a more intuitive depiction of the intricate variation patterns of $R/T$ coefficients, aligning with the observed characteristics evident in previous visualizations.

## 4. Discussion

We have derived exact $R/T$ coefficient formulas at an imperfectly welded contact interface, delineating the influence of in-situ horizontal stress on the interaction between two HTI media. These formulas elucidate the intricate interplay among in-situ horizontal stress, frequency, and $R/T$ response at the interface separating two distinct HTI media. Through numerical analysis, we have discerned how in-situ horizontal stress impacts the phase velocity of P waves, the elastic anisotropy of stressed HTI media, and the variations of $R/T$ coefficients with stress and frequency. This comprehensive understanding contributes to the comprehension of seismic wave propagation in stressed HTI media. In future research endeavors, the exact $R/T$ coefficient formulas can be integrated into seismic

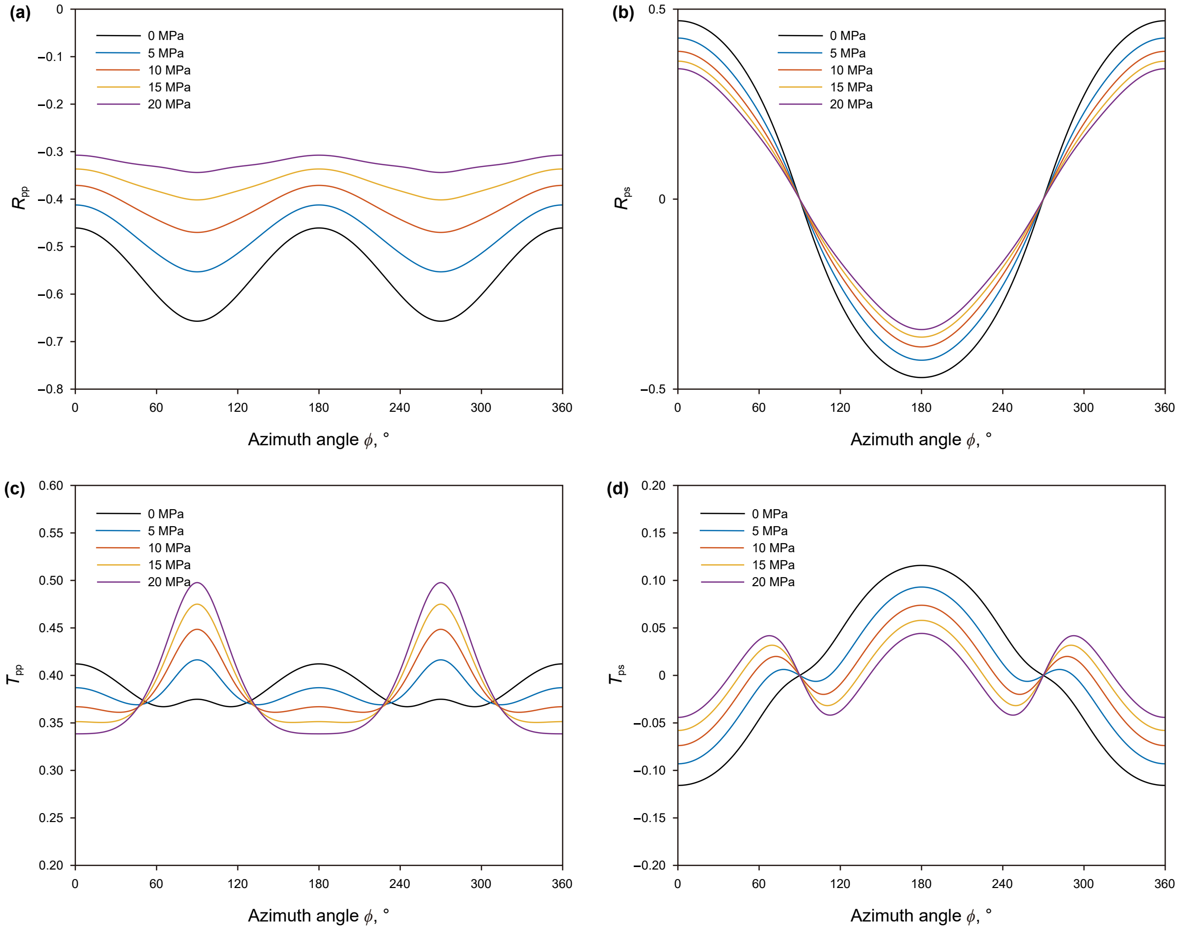

**Fig. 12.** Diagram of $R/T$ coefficients varying with in-situ horizontal stress and azimuth angle **(a)** $R_{pp}$ **(b)** $R_{ps}$ **(c)** $T_{pp}$ **(d)** $T_{ps}$ (The frequency is 30 Hz, and the incident angle is 30°).

AVO inversion methodologies (Chen and Zong, 2022) and the prediction of real underground stress fields (Chen et al., 2023c; Yang et al., 2023) within stressed anisotropic strata.

However, we only consider the effect of in-situ horizontal stress on the aperture of imperfectly welded contact (e.g. average aperture $d$), which is an ideal assumption, while the stress situation of the actual stratum is much more complicated, and stress can also affect the magnitude of $r^{\mathrm{w}}$ and $d^*$, so the more reasonable physical mechanism should be explored to modify our model in future studies.

Additionally, it is imperative to acknowledge that real strata are generally heterogeneous or porous and filled with fluid, all of which can significantly influence seismic wave propagation under stress. These factors necessitate consideration in future investigations. Our formulated equations offer foundational insights into deriving R/T coefficient formulas between more complex media at the imperfectly welded contact interface within the Earth's interior, including rocks subjected to orthogonal stresses and rocks featuring tilted transversely isotropic (TTI) symmetry.

## 5. Conclusions

The principal objective of this investigation is to establish exact $R/T$ coefficient formulas governing seismic wave propagation at an imperfectly welded contact interface between two distinct HTI media, under the influence of in-situ horizontal stress. These formulations provide invaluable insights into elucidating azimuth-dependent seismic response characteristics in the presence of stress. By delineating the intricate relationship between $R/T$ coefficients and in-situ horizontal stress at an imperfectly welded contact interface, a profound understanding of seismic behavior within HTI media can be attained. Initiating the analysis, we rigorously establish exact boundary conditions employing the generalized stress-strain relationship and the linear-slip theory at an imperfectly welded contact interface, and explore the influence of in-situ horizontal stress on imperfectly welded contact interface at the same time. Subsequent derivation yields exact $R/T$ coefficient formulations at this interface, delineating its separation between two HTI media. Numerical analyses reveal that density, wave velocity, and anisotropy within an HTI medium exhibit pronounced sensitivity to stress, exhibiting alterations across different media. Notably, at sufficiently large incident angles, $R/T$ coefficients evince heightened sensitivity to influencing factors. These formulations and associated modeling outcomes hold significant utility for fracture characterization, inversion of stress-related parameters, and the detection of in-situ stress within subsurface hydrocarbon reservoirs.

## CRediT authorship contribution statement

**Xin-Peng Pan:** Writing – review & editing. **Cheng-Xu Lu:** Writing – review & editing, Writing – original draft. **Hao-Wen Xu:** Visualization, Validation. **Da-Zhou Zhang:** Visualization, Validation.

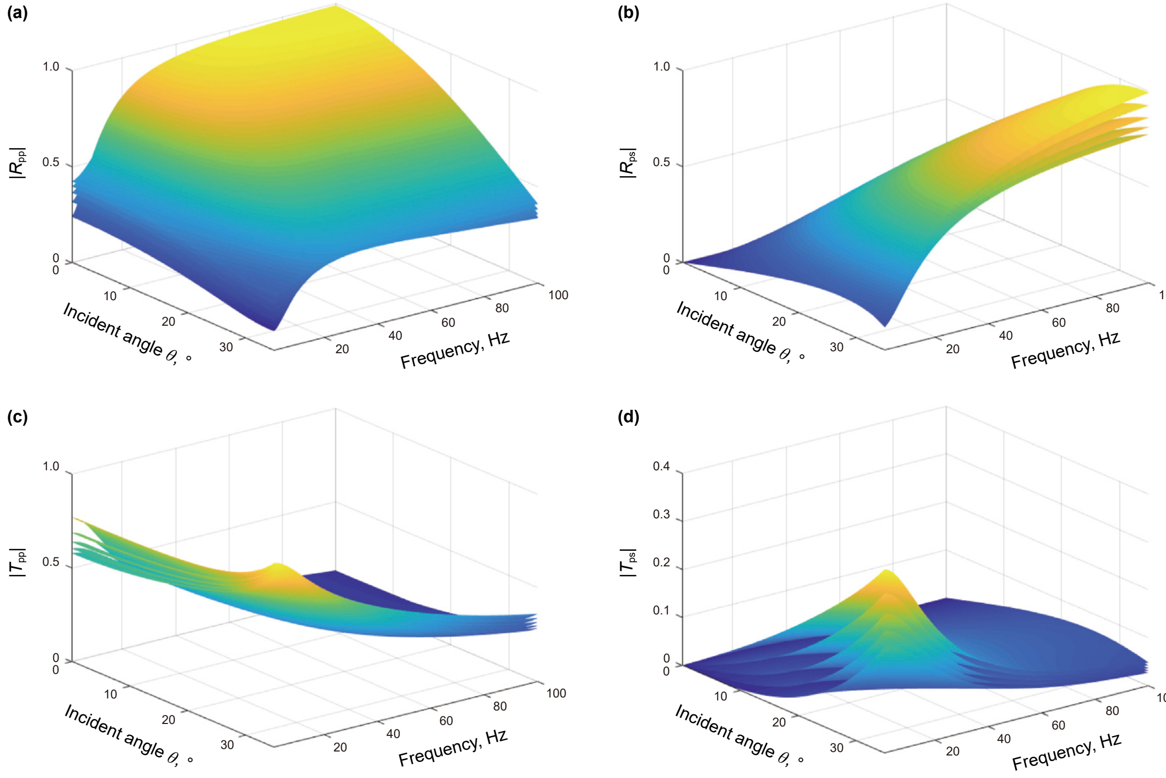

**Fig. 13.** Diagram of $R/T$ coefficients varying with in-situ horizontal stress, incident angle and frequency **(a)** $|R_{\mathrm{pp}}|$ **(b)** $|R_{\mathrm{ps}}|$ **(c)** $|T_{\mathrm{pp}}|$ **(d)** $|T_{\mathrm{ps}}|$ (The azimuth angle is 0°).

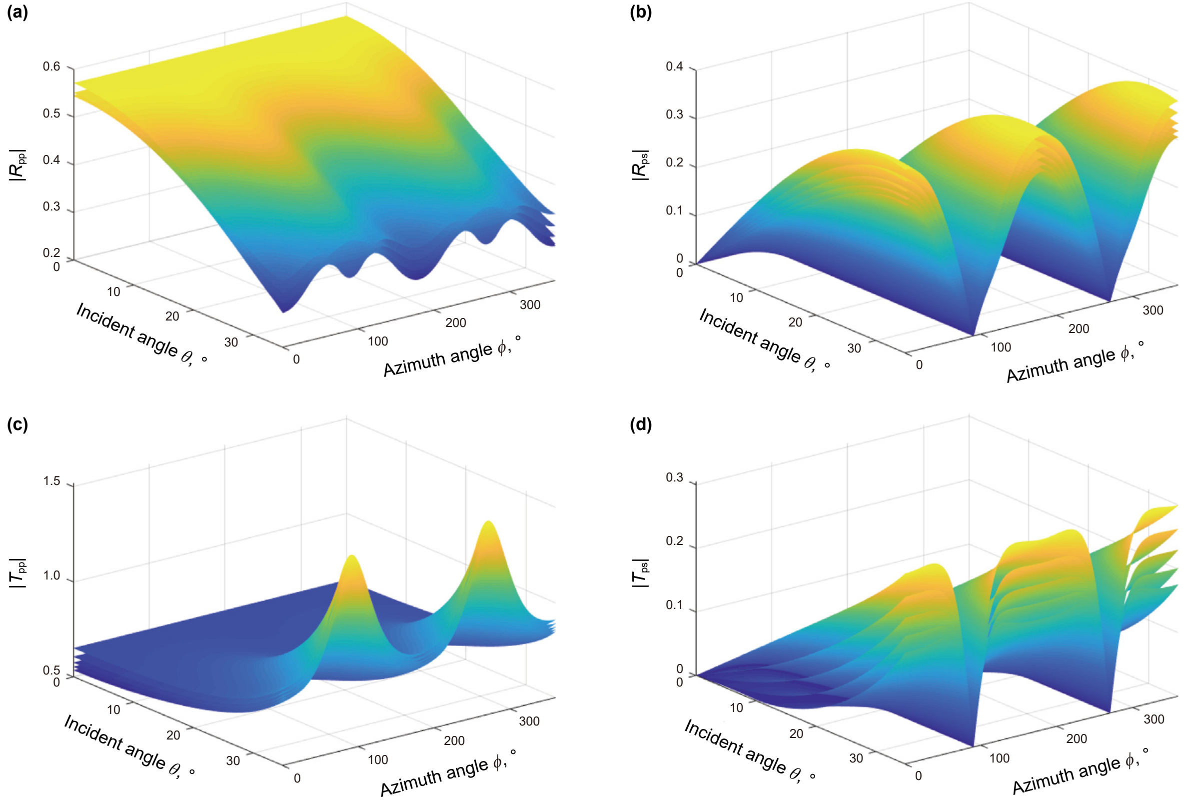

**Fig. 14.** Diagram of 3D seismic response characteristics **(a)** $|R_{\mathrm{pp}}|$ **(b)** $|R_{\mathrm{ps}}|$ **(c)** $|T_{\mathrm{pp}}|$ **(d)** $|T_{\mathrm{ps}}|$ (The frequency is 10 Hz).

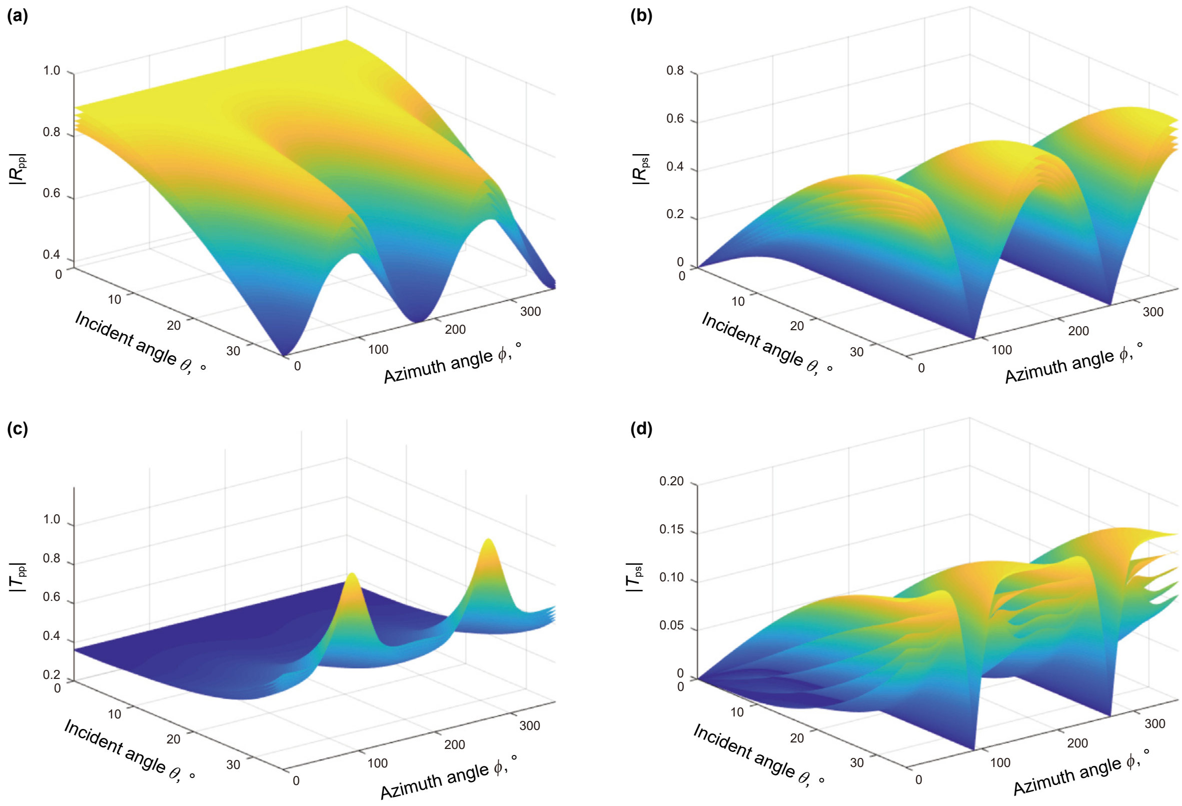

**Fig. 15.** Diagram of 3D seismic response characteristics **(a)** $|R_{\mathrm{pp}}|$ **(b)** $|R_{\mathrm{ps}}|$ **(c)** $|T_{\mathrm{pp}}|$ **(d)** $|T_{\mathrm{ps}}|$ (The frequency is 30 Hz).

## Data availability statement

Data and codes utilized in the study are available from the corresponding author upon reasonable request.

## Acknowledgements

We would like to express our gratitude to the sponsorship of the National Natural Science Foundation of China (42474172, 42130810), the Science and Technology Innovation Program of Hunan Province (2022RC1238), the Natural Science Foundation of Hunan Province (2025JJ20036, 2023JJ30663), and the Changzhou Science and Technology Support Project (CE20235069) for the funding in this research. We also thank all the editors and reviewers for a thorough reading and many constructive comments on this article, and we are grateful for resources from the High-Performance Computing Center of Central South University.

## Appendix A. Acoustoelasticity stiffness tensor of HTI media under in-situ horizontal stress

This appendix presents the acoustoelastic stiffness tensor for an HTI medium under the in-situ horizontal stress. The displacement increment $U_\alpha(X,t)$ caused by seismic wave perturbation, transitioning from the initial to the final state, is given as

$$U_\alpha(X,t)=U_\alpha^{\mathrm{f}}-U_\alpha^0=x_\alpha-\xi_\alpha. \tag{A-1}$$

Assuming the seismic wave disturbance is infinitesimal, the deformation increment is

$$E_{\alpha\beta}=\frac{1}{2}\left(U_{\alpha,\beta}+U_{\beta,\alpha}+U^0_{\gamma,\alpha}U_{\gamma,\beta}+U^0_{\gamma,\beta}U_{\gamma,\alpha}\right). \tag{A-2}$$

The internal energy function of hyperelastic rock establishes the constitutive equation. By neglecting higher-order terms (Pao, 1984), the equation becomes

$$T_{\alpha\beta}=c_{\alpha\beta\gamma\delta}E_{\gamma\delta}+c_{\alpha\beta\gamma\delta\varepsilon\eta}e^0_{\gamma\delta}e_{\varepsilon\eta}, \tag{A-3}$$

where $c_{\alpha\beta\gamma\delta}$ and $c_{\alpha\beta\gamma\delta\varepsilon\eta}$ denote the second-order and third-order elastic modulus (2oEM and 3oEM) tensor of HTI medium, respectively. Using Voigt's notation, we simplify this as follows:

$$T_{\alpha\beta}=\Omega_{\alpha\beta\gamma\delta}U_{\gamma,\delta}, \tag{A-4}$$

with

$$\Omega_{\alpha\beta\gamma\delta}=c_{\alpha\beta\gamma\delta}\left(1-e^0_{\eta\eta}\right)+c_{\varepsilon\beta\gamma\delta}U^0_{\alpha,\varepsilon}+c_{\alpha\varepsilon\gamma\delta}U^0_{\beta,\varepsilon}+c_{\alpha\beta\varepsilon\delta}U^0_{\gamma,\varepsilon}+c_{\alpha\beta\gamma\varepsilon}U^0_{\delta,\varepsilon}+c_{\alpha\beta\gamma\delta\varepsilon\eta}e^0_{\varepsilon\eta}. \tag{A-5}$$

Since the predeformation is static, the motion equation for rock particles, with displacement increments due to seismic disturbances, is expressed as

$$H_{\alpha\beta\gamma\delta}U_{\gamma,\beta\delta}=\rho\ddot{U}_\alpha, \tag{A-6}$$

with

$$H_{\alpha\beta\gamma\delta}=\Omega_{\alpha\beta\gamma\delta}+\sigma^0_{\beta\delta}\delta_{\alpha\gamma}, \tag{A-7}$$

where $\sigma^0_{\beta\delta}$ represents the initial stress in the HTI media. Given significant difference in magnitudes between $\sigma^0_{\beta\delta}$, $c_{\alpha\beta\gamma\delta}$, and $c_{\alpha\beta\gamma\delta\varepsilon\eta}$, we approximate $|c_{\alpha\beta\gamma\delta\varepsilon\eta}| \gg |c_{\alpha\beta\gamma\delta}| \gg |\sigma^0_{\beta\delta}|$ (Prioul et al., 2004), reducing Eq. (A-8) to

$$H_{\alpha\beta\gamma\delta} = c_{\alpha\beta\gamma\delta} + c_{\alpha\beta\gamma\delta\varepsilon\eta} e^0_{\varepsilon\eta}. \tag{A-8}$$

For an HTI medium under in-situ horizontal stress, the acoustoelastic stiffness tensor $H_{\alpha\beta\gamma\delta}$, using Voigt notation, is represented as

$$H_{\alpha\beta} = \begin{bmatrix} H_{11} & H_{12} & H_{13} & 0 & 0 & 0 \\ H_{12} & H_{22} & H_{23} & 0 & 0 & 0 \\ H_{13} & H_{23} & H_{33} & 0 & 0 & 0 \\ 0 & 0 & 0 & H_{44} & 0 & 0 \\ 0 & 0 & 0 & 0 & H_{55} & 0 \\ 0 & 0 & 0 & 0 & 0 & H_{66} \end{bmatrix}, \tag{A-9}$$

where

$$H_{11} = c_{11} + c_{111} e^0_{xx} + (c_{112} + c_{133}) e^0_{yy}, \tag{A-10}$$

$$H_{12} = H_{13} = c_{13} + c_{112} e^0_{xx} + (c_{123} + c_{133}) e^0_{yy}, \tag{A-11}$$

$$H_{23} = c_{23} + c_{123} e^0_{xx} + (c_{112} + c_{113}) e^0_{yy}, \tag{A-12}$$

$$H_{22} = H_{33} = c_{33} + c_{112} e^0_{xx} + (c_{111} + c_{113}) e^0_{yy}, \tag{A-13}$$

$$H_{44} = c_{44} + c_{144} e^0_{xx} + (c_{155} + c_{344}) e^0_{yy}, \tag{A-14}$$

$$H_{55} = H_{66} = c_{66} + c_{155} e^0_{xx} + (c_{144} + c_{344}) e^0_{yy}. \tag{A-15}$$

with (Goldberg, 1961)

$$c_{111} = 2A + 6B + 2C, \tag{A-16}$$

$$c_{144} = B, \tag{A-17}$$

$$c_{112} = c_{133} = c_{122} = 2B + 2C, \tag{A-18}$$

$$c_{155} = c_{344} = \frac{1}{2}A + B, \tag{A-19}$$

$$c_{123} = 2C. \tag{A-20}$$

The vertical P- and S-wave velocities (Thomsen, 1986) of the HTI media is derived from Eq. (A-9) as

$$V^2_{\mathrm{P0}} = H_{33} \big/ \rho, \tag{A-21}$$

$$V^2_{\mathrm{S0}} = H_{44} \big/ \rho, \tag{A-22}$$

Similarly, the Tsvankin-type anisotropic parameters $\varepsilon^{(\mathrm{v})}$, $\delta^{(\mathrm{v})}$, and $\gamma^{(\mathrm{v})}$ in weakly anisotropic HTI media (Tsvankin, 1997) can be expressed as

$$\varepsilon^{(\mathrm{v})} = \frac{H_{11} - H_{33}}{2H_{33}}, \tag{A-24}$$

$$\delta^{(\mathrm{v})} = \frac{(H_{13} + H_{66})^2 - (H_{33} - H_{66})^2}{2H_{33}(H_{33} - H_{66})} \approx \frac{H_{13} - H_{33} + 2H_{66}}{2H_{33}}, \tag{A-25}$$

$$\gamma^{(\mathrm{v})} = \frac{H_{66} - H_{44}}{2H_{44}}. \tag{A-26}$$

In traditional linear elastic theory, potential energy is a quadratic function of strain. However, acoustoelastic theory incorporates third-order elastic constants to account for variations in acoustic properties under stress. This nonlinear elastic framework forms the basis for studying stress-induced anisotropy, mapping any axial in-situ stress field to the anisotropic stiffness tensor.

## Appendix B. Stress-dependent characteristics of imperfectly welded contact interface

In this appendix, we present the stress-dependent characteristics of an imperfectly welded contact interface. Based on previous assumptions, the parameters $Z_{\mathrm{T}}$ and $Z_{\mathrm{N}}$ can be expressed in terms of the intrinsic fracture parameters and background elastic parameters (Worthington and Lubbe, 2007) as follows:

$$\frac{1}{Z_{\mathrm{N}}} = r^{\mathrm{w}} \frac{4\mu^*}{\pi d^*} \left(1 - \frac{V^2_{\mathrm{S0}}}{V^2_{\mathrm{P0}}}\right) \left\{1 + \frac{2(r^{\mathrm{w}})^{1/2}}{\sqrt{\pi}}\right\} + \frac{K + (4/3)\mu}{d}, \tag{B-1}$$

$$\frac{1}{Z_{\mathrm{T}}} = r^{\mathrm{w}} \frac{8\mu^*}{\pi d^*} \frac{\left(1 - V^2_{\mathrm{S0}} \big/ V^2_{\mathrm{P0}}\right)}{\left(3 - 2V^2_{\mathrm{S0}} \big/ V^2_{\mathrm{P0}}\right)} \left\{1 + \frac{2(r^{\mathrm{w}})^{1/2}}{\sqrt{\pi}}\right\} + \frac{\mu}{d}, \tag{B-2}$$

where $V_{\mathrm{P0}}$, $V_{\mathrm{S0}}$, and $\mu^*$ represent the P-wave velocity, S-wave velocity and shear modulus of the unstressed background medium, respectively. Parameters $d^*$, $r^{\mathrm{w}}$, and $d$ correspond to the average radius of the welded contact areas, the ratio of welded contact to the fracture area, and the average aperture of the imperfectly welded contact interface, respectively. Additionally, $\mu$ and $K$ denote the shear and bulk moduli of the filler material in the non-welded interface, respectively. For field application, $r^{\mathrm{w}}$ can often be approximated as 0, allowing Eqs. (B-1) and (B-2) to be simplified as

$$Z_{\mathrm{N}} = \frac{K + (4/3)\mu}{d}, \tag{B-3}$$

$$Z_{\mathrm{T}} = \frac{\mu}{d}. \tag{B-4}$$

In this study, we consider the stress-dependent variation of the average aperture $d$. Under conditions of moderate stress, its dependence follows generalized Hooke's law, indicating that the change in $d$ is inversely proportional to stress. The influence of stress on $d^*$ and $r^{\mathrm{w}}$ is neglected. As such, the effects of stress on $Z_{\mathrm{T}}$ and $Z_{\mathrm{N}}$ can be modeled based on the given values of $d^*$ and $r^{\mathrm{w}}$.

## Appendix C. Exact P-wave *R*/*T* coefficient formulas in HTI media under in-situ horizontal stress

In this appendix, we present the exact P-wave *R*/*T* coefficient formulas in HTI media under in-situ horizontal stress. The elements in Eq. (10) are expressed as follows:

$$\boldsymbol{\Gamma}=\begin{bmatrix}\Gamma_{11} & \Gamma_{12} & \Gamma_{13} & \Gamma_{14}\\ \Gamma_{21} & \Gamma_{22} & \Gamma_{23} & \Gamma_{24}\\ \Gamma_{31} & \Gamma_{32} & \Gamma_{33} & \Gamma_{34}\\ \Gamma_{41} & \Gamma_{42} & \Gamma_{43} & \Gamma_{44}\end{bmatrix}, \tag{C-1}$$

$$\boldsymbol{\Lambda}=\begin{bmatrix}R_{\mathrm{pp}} & R_{\mathrm{ps}} & T_{\mathrm{pp}} & T_{\mathrm{ps}}\end{bmatrix}^{\mathrm{T}}, \tag{C-2}$$

$$\mathbf{M}=\begin{bmatrix}\mathrm{M}_{11} & \mathrm{M}_{21} & \mathrm{M}_{31} & \mathrm{M}_{41}\end{bmatrix}^{\mathrm{T}}. \tag{C-3}$$

where

$$\Gamma_{11}=-\mathrm{M}_{11}=p_1V_{\mathrm{PP}}\cos\varphi,\Gamma_{12}=q_2V_{\mathrm{PS}}, \tag{C-4}$$

$$\Gamma_{13}=-p_3V_{\mathrm{PP}'}\cos\varphi+j\omega Z_{\mathrm{T}}p_3q_3V_{\mathrm{PP}'}\cos\varphi\left(2H_{66}+\sigma_{xx}^0\right), \tag{C-5}$$

$$\Gamma_{14}=q_4V_{\mathrm{PS}'}+j\omega Z_{\mathrm{T}}V_{\mathrm{PS}'}\left[H_{66}\left(p_4^2\cos^2\varphi-q_4^2\right)+\sigma_{xx}^0p_4^2\cos^2\varphi\right], \tag{C-6}$$

$$\Gamma_{21}=\mathrm{M}_{21}=q_1V_{\mathrm{PP}},\Gamma_{22}=-p_2V_{\mathrm{PS}}\cos\varphi, \tag{C-7}$$

$$\Gamma_{23}=q_3V_{\mathrm{PP}'}-j\omega Z_{\mathrm{N}}V_{\mathrm{PP}'}\left(H_{13}p_3^2\cos^2\varphi+H_{33}q_3^2\right), \tag{C-8}$$

$$\Gamma_{24}=p_4V_{\mathrm{PS}'}\cos\varphi-j\omega Z_{\mathrm{N}}p_4q_4V_{\mathrm{PS}'}\cos\varphi(H_{33}-H_{13}), \tag{C-9}$$

$$\Gamma_{31}=\mathrm{M}_{31}=p_1q_1V_{\mathrm{PP}}^2\cos\varphi\left(2H'_{66}+\sigma_{xx}^0\right), \tag{C-10}$$

$$\Gamma_{32}=-H'_{66}V_{\mathrm{PP}}V_{\mathrm{PS}}\left(q_2^2-p_2^2\cos^2\varphi\right)-\sigma_{xx}^0V_{\mathrm{PP}}V_{\mathrm{PS}}p_2^2\cos^2\varphi, \tag{C-11}$$

$$\Gamma_{33}=p_3q_3V_{\mathrm{PP}}V_{\mathrm{PP}'}\cos\varphi\left(2H_{66}+\sigma_{xx}^0\right), \tag{C-12}$$

$$\Gamma_{34}=-H_{66}V_{\mathrm{PP}}V_{\mathrm{PS}'}\left(q_4^2-p_4^2\cos^2\varphi\right)+\sigma_{xx}^0V_{\mathrm{PP}}V_{\mathrm{PS}'}p_4^2\cos^2\varphi, \tag{C-13}$$

$$\Gamma_{41}=-\mathrm{M}_{41}=H'_{13}p_1^2V_{\mathrm{PP}}^2\cos^2\varphi+H'_{33}q_1^2V_{\mathrm{PP}}^2, \tag{C-14}$$

$$\Gamma_{42}=-p_2q_2V_{\mathrm{PP}}V_{\mathrm{PS}}\cos\varphi(H'_{13}-H'_{33}), \tag{C-15}$$

$$\Gamma_{43}=-V_{\mathrm{PP}}V_{\mathrm{PP}'}\left(H_{13}p_3^2\cos^2\varphi+H_{33}q_3^2\right), \tag{C-16}$$

$$\Gamma_{44}=-p_4q_4V_{\mathrm{PP}}V_{\mathrm{PS}'}\cos\varphi(H_{33}-H_{13}). \tag{C-17}$$

and

$$R_{\mathrm{pp}}=\frac{A_1}{A_0},R_{\mathrm{ps}}=\frac{A_2}{A_0}\frac{V_{\mathrm{PP}}}{V_{\mathrm{PS}}},T_{\mathrm{pp}}=\frac{A_3}{A_0}\frac{V_{\mathrm{PP}}}{V_{\mathrm{PP}'}},T_{\mathrm{ps}}=\frac{A_4}{A_0}\frac{V_{\mathrm{PP}}}{V_{\mathrm{PS}'}}. \tag{C-18}$$

In these equations, $H'$ and $H$ represent the effective acoustoelastic stiffness tensors of the upper and lower media, respectively. The subscripts PP, PS, PP′, and PS′ represent the four types of scattered waves. Additionally, $p_i$ and $q_i$ $(i=1,2,3,4)$ denote the horizontal and vertical wavenumber, respectively, while the indices $i$ refer to the four types of reflected and transmitted waves.

## References

Abiza, Z., Destrade, M., Ogden, R.W., 2012. Large acoustoelastic effect. Wave Motion 49 (2), 364–374. https://doi.org/10.1016/j.wavemoti.2011.12.002.

Aki, K., Richards, P.G., 1980. Quantitative Seismology: Theory and Methods. W.H. Freeman and Company. https://www.amazon.com/Quantitative-Seismology-Keiiti-Aki/dp/1891389637.

Ba, J., Carcione, J.M., Cao, H., 2013. Poro-acoustoelasticity of fluid-saturated rocks. Geophys. Prospect. 61 (3), 599–612. https://doi.org/10.1111/j.1365-2478.2012.01091.x.

Bakulin, A., Sinha, B., Prioul, R., 2003. System and method for estimating subsurface principal stresses from seismic reflection data. US Patent application publication, US 2003/0125878 A1, https://www.freepatentsonline.com/20030125878.pdf.

Biot, M.A., 1956a. Theory of propagation of elastic waves in a fluid-saturated porous solid. II. Higher frequency range. J. Acoust. Soc. Am. 28 (2), 179–191. https://doi.org/10.1121/1.1908241.

Biot, M.A., 1956b. Thermoelasticity and irreversible thermodynamics. J. Appl. Phys. 27 (3), 240–253. https://doi.org/10.1063/1.1722351.

Carcione, J.M., 2015. Wave fields in real media: wave propagation in anisotropic, anelastic, porous and electromagnetic media. Handbook of Geophysical Exploration, third ed. Elsevier Ltd, Amsterdam. https://doi.org/10.1016/s0950-1401(07)x8002-9.

Chapman, M., 2009. Modeling the effect of multiple sets of mesoscale fractures in porous rock on frequency-dependent anisotropy. Geophysics 74 (6), 1ND–Z107. https://doi.org/10.1190/1.3204779.

Chaisri, S., Krebes, E.S., 2000. Exact and approximate formulas for P-SV reflection and transmission coefficients for a nonwelded contact interface. J. Geophys. Res. Solid Earth 105 (B12), 28045–28054. https://doi.org/10.1029/2000JB900296.

Chen, F.B., Zong, Z.Y., Jiang, M., 2021. Seismic reflectivity and transmissivity parametrization with the effect of normal in-situ stress. Geophys. J. Int. 226 (3), 1599–1614. https://doi.org/10.1093/gji/ggab179.

Chen, F.B., Zong, Z.Y., Yin, X.Y., 2022a. Acoustothermoelasticity for joint effects of stress and thermal fields on wave dispersion and attenuation. J. Geophys. Res. Solid Earth 127 (4), e2021JB023671. https://doi.org/10.1029/2021JB023671.

Chen, F.B., Zong, Z.Y., Yin, X.Y., 2022b. Accurate formulae for P-wave reflectivity and transmissivity for a non-welded continuous interface with the effect of in-situ vertical stress. Geophys. J. Int. 229 (1), 311–327. https://doi.org/10.1093/gji/ggab475.

Chen, F.B., Zong, Z.Y., 2022. PP-wave reflection coefficient in stress-induced anisotropic media and amplitude variation with incident angle and azimuth inversion. Geophysics 87 (6), C155–C172. https://doi.org/10.1190/geo2021-0706.1.

Chen, F.B., Zong, Z.Y., Stovas, A., 2023a. Wave reflection and transmission coefficients for layered transversely isotropic media with vertical symmetry axis under initial stress. Geophys. J. Int. 233 (3), 1580–1595. https://doi.org/10.1093/gji/ggad011.

Chen, F.B., Zong, Z.Y., Yin, X.Y., Stovas, A., 2023b. Stress dependence of elastic wave dispersion and attenuation in fluid-saturated porous layered media. Sci. China Earth Sci. 53 (11), 2669–2681. https://doi.org/10.1007/s11430-022-1147-7.

Chen, F.B., Zong, Z.Y., Yin, X.Y., 2023c. Monitoring the change in horizontal stress with multi-wave time-lapse seismic response based on nonlinear elasticity theory. Pet. Sci. 20 (2), 815–826. https://doi.org/10.1016/j.petsci.2022.09.022.

Cheng, A.H.D., 2016. Porochemoelasticity. In: Theory and Applications of Transport in Porous Media, vol. 27. Springer International Publishing, Switzerland. https://www.springer.com/series/6612.

Cui, X., Krebes, E.S., Lines, L.R., 2017. Seismic inversion for geologic fractures and fractured media. Geophysics 82 (5), 1SO–Z39. https://doi.org/10.1190/geo2016-0123.1.

Degtyar, A.D., Rokhlin, S.I., 1998. Stress effect on boundary conditions and elastic wave propagation through an interface between anisotropic media. J. Acoust. Soc. Am. 104 (4), 1992–2003. https://doi.org/10.1121/1.423765.

Fu, L.Y., Fu, B.Y., Sun, W.J., Han, T.C., Liu, J.L., 2020. Elastic wave propagation and scattering in prestressed porous rocks. Sci. China Earth Sci. 63 (9), 1309–1329. https://doi.org/10.1007/s11430-019-9615-3.

Goldberg, Z.A., 1961. Interaction of plane longitudinal and transverse elastic waves. Sov. Phys. Acoust. 6, 306–310. https://www.researchgate.net/publication/302560025.

Guo, Z.Q., Liu, X.W., Fu, W., Li, X.Y., 2015. Modeling and analysis of azimuthal AVO responses from a viscoelastic anisotropic reflector. Appl. Geophys. 12 (3), 441–452. https://doi.org/10.1007/s11770-015-0498-9.

Guo, Z.Q., Li, X.Y., 2017. Azimuthal AVO signatures of fractured poroelastic sandstone layers. Explor. Geophys. 48 (1), 56–66. https://doi.org/10.1071/EG15050.

Huang, X.J., Burns, D.R., Toksöz, M.N., 2001. The effect of stresses on the sound velocity in rocks: theory of Acoustoelasticity and Experimental Measurements. https://dspace.mit.edu/handle/1721.1/68599.

Hughes, D.S., Kelly, J.L., 1953. Second-order elastic deformation of solids. Phys. Rev. 92 (5), 1145. https://doi.org/10.1103/PhysRev.92.1145.

Hou, W.T., Fu, L.Y., Wei, J., Wang, Z.W., 2021. Characteristics of wave propagation in thermoelastic media. Chin. J. Geophys. 64 (4), 1364–1374. https://doi.org/10.6038/cjg2021N0458.

Innanen, K.A., 2011. Inversion of the seismic AVF/AVA signatures of highly attenuative targets. Geophysics 76 (1), 1JF–Z19. https://doi.org/10.1190/1.3518816.

Johnson, P.A., Rasolofosaon, P.N.J., 1996. Nonlinear elasticity and stress-induced anisotropy in rocks. J. Geophys. Res. 101 (B2), 3113–3124. https://doi.org/

10.1029/95JB02880.

Li, X.W., Guo, Z.Q., Han, X., 2018. Full waveform seismic AVAZ signatures of anisotropic shales by integrated rock physics and the reflectivity method. J. Geophys. Eng. 15 (3), 980–994. https://doi.org/10.1088/1742-2140/aaa3d3.

Li, Y.D., Guo, Z.Q., Liu, C., 2024. Characterization of fluid-saturated fractures based on seismic azimuthal anisotropy dispersion inversion method. IEEE Trans. Geosci. Rem. Sens. 62, 1–17. https://doi.org/10.1109/TGRS.2024.3407134.

Liu, J.X., Cui, Z.W., Wang, K.X., 2007. Reflection and transmission of acoustic waves at the interface between rocks in the presence of elastic–plastic deformations. J. Geophys. Eng. 4 (2), 232–241. https://doi.org/10.1088/1742-2132/4/2/012.

Liu, J.X., Cui, Z.W., Wang, K.X., 2009. The relationships between uniaxial stress and reflection coefficients. Geophys. J. Int. 179 (3), 1584–1592. https://doi.org/10.1111/j.1365-246X.2009.04353.x.

Liu, J.X., Cui, Z.W., Wang, K.X., 2016. Relationships between uniaxial stress and S-wave reflection coefficients. Chin. J. Geophys. 59 (4), 1469–1476. https://doi.org/10.6038/cjg20160427.

Liu, J.X., Cui, Z.W., Igor, S., 2021. Effect of stresses on wave propagation in fluid-saturated porous media. Int. J. Eng. Sci. 167, 103519. https://doi.org/10.1016/j.ijengsci.2021.103519.

Lu, N., Liu, C., Guo, Z.Q., Liu, X.W., 2018. Azimuthal seismic responses from shale formation based on anisotropic rock physics and reflectivity method. Explor. Geophys. 49, 363–371. https://doi.org/10.1071/EG16097.

Malehmir, R., Schmitt, D.R., 2017. Acoustic reflectivity from variously oriented orthorhombic media: analogies to seismic responses from a fractured anisotropic crust. J. Geophys. Res. Solid Earth 122 (12), 10069–10085. https://doi.org/10.1002/2017JB014160.

Norris, A.N., 1995. The speed of a wave along a fluid/solid interface in the presence of anisotropy and prestress. J. Acoust. Soc. Am. 98 (2), 1147–1154. https://doi.org/10.1121/1.413613.

Pan, X.P., Zhang, G.Z., Yin, X.Y., 2018. Azimuthally pre-stack seismic inversion for orthorhombic anisotropy driven by rock physics. Sci. China Earth Sci. 61, 425–440. https://doi.org/10.1007/s11430-017-9124-6.

Pan, X.P., Lu, C.X., Zhao, Z.Z., Liu, J.X., 2024. Characteristics of orthorhombic anisotropic seismic response induced by horizontal in situ stress in vertical transversely isotropic media. Sci. China. Earth. Science 67, 2291–2310. https://doi.org/10.1007/s11430-023-1294-4.

Pan, X.P., Zhang, G.Z., 2019. Bayesian seismic inversion for estimating fluid content and fracture parameters in a gas-saturated fractured porous reservoir. Sci. China Earth Sci. 62, 798–811. https://doi.org/10.1007/s11430-018-9284-2.

Pan, X.P., Zhang, G.Z., Cui, Y., 2020. Matrix-fluid-fracture decoupled-based elastic impedance variation with angle and azimuth inversion for fluid modulus and fracture weaknesses. J. Petrol. Sci. Eng. 189, 106974. https://doi.org/10.1016/j.petrol.2020.106974.

Pan, X.P., Zhao, Z.Z., Zhang, D.Z., 2023. Characteristics of azimuthal seismic reflection response in horizontal transversely isotropic media under In-situ horizontal stress. Surv. Geophys. 44, 387–423. https://doi.org/10.1007/s10712-022-09739-8.

Pao, Y.H., 1984. Acoustoelasticity and ultrasonic measurement of residual stress. Phys. Acoust. 61–143. https://www.mendeley.com/catalogue.

Prioul, R., Bakulin, A., Bakulin, V., 2004. Nonlinear rock physics model for estimation of 3D subsurface stress in anisotropic formations: theory and laboratory verification. Geophysics 69 (2), 415–425. https://doi.org/10.1190/1.1707061.

Pšenčik, I., Vavryčuk, V., 1998. Weak contrast PP-wave displacement R/T coefficients in weakly anisotropic elastic media. Pure. Appl. Geophys. 151, 699–718. https://doi.org/10.1007/s000240050137.

Pšenčik, I., Martins, J.L., 2001. Properties of weak contrast PP refection/transmission coefficients for weakly anisotropic elastic media. Studia Geophys. Geod. 45 (2), 176–199. https://doi.org/10.1023/A:1021868328668.

Pyrak-Nolte, L.J., Myer, L.R., Cook, N.G.W., 1990. Transmission of seismic waves across single natural fractures. J. Geophys. Res. Solid Earth 95 (B6), 8617–8638. https://doi.org/10.1029/JB095iB06p08617.

Rüger, A., 1997. P-wave refection coefficients for transversely isotropic models with vertical and horizontal axis of symmetry. Geophysics 62, 713–722. https://doi.org/10.1190/1.1444181.

Sarkar, D., Bakulin, A., Kranz, R.L., 2003. Anisotropic inversion of seismic data for stressed media: theory and a physical modeling study on Berea Sandstone. Geophysics 68 (2), 690–704. https://doi.org/10.1190/1.1567240.

Schoenberg, M., 1980. Elastic wave behavior across linear slip interfaces. J. Acuost. Soc. Am. 68 (5), 1516–1521. https://doi.org/10.1121/1.385077.

Schoenberg, M., Douma, J., 1988. Elastic wave propagation in media with parallel fractures and aligned cracks. Geophys. Prospect. 36 (6), 571–590. https://doi.org/10.1111/j.1365-2478.1988.tb02181.x.

Schoenberg, M., Protázio, J., 1990. 'Zoeppritz' rationalized and generalized to anisotropy media. J. Acoust. Soc. Am. 88 (S1), S46. https://doi.org/10.1121/1.2029011.

Sinha, B.K., Kostek, S., Norris, A.N., 1995. Stoneley and flexural modes in pressurized boreholes. J. Geophys. Res. Solid Earth 100 (B11), 22375–22381. https://doi.org/10.1029/95JB02504.

Sinha, B.K., Kostek, S., 1996. Stress-induced azimuthal anisotropy in borehole flexural waves. Geophysics 61 (6), 1899–1907. https://doi.org/10.1190/1.1444105.

Sinha, B.K., Kane, M.R., Bernard, F., 2000. Dipole dispersion crossover and sonic logs in a limestone reservoir. Geophysics 65 (2), 390–407. https://doi.org/10.1190/1.1444734.

Sinha, B.K., Plona, T.J., 2001. Wave propagation in rocks with elastic-plastic deformations. Geophysics 66 (3), 772–785. https://doi.org/10.1190/1.1444967.

Stovas, A., Ursin, B., 2003. Reflection and transmission responses of layered transversely isotropic viscoelastic media. Geophys. Prospect. 51, 447–477. https://doi.org/10.1046/j.1365-2478.2003.00381.x.

Sun, Y.Y., Gurevich, B., 2020. Modeling the effect of pressure on the moduli dispersion in fluid-saturated rocks. J. Geophys. Res. Solid Earth 125 (8), e2019JB019297. https://doi.org/10.1029/2019JB019297.

Thomsen, L., 1986. Weak elastic anisotropy. Geophysics 51 (10), 1954–1966. https://doi.org/10.1190/1.1442051.

Tsvankin, I., 1997. Anisotropic parameters and P-wave velocity for orthorhombic media. Geophysics 62 (4), 1292–1309. https://doi.org/10.1190/1.1444231.

Worthington, M.H., Lubbe, R., 2007. The scaling of fracture compliance. Geol. Soc., Lond., Spec. Publ. 270, 73–82. https://doi.org/10.1144/GSL.SP.2007.270.01.05.

Winkler, K., Liu, X., 1996. Measurements of third-order elastic constants in rocks. J. Acoust. Soc. Am. 100, 1392–1398. https://doi.org/10.1121/1.415986.

Winkler, K.W., Sinha, B.K., Plona, T.J., 1998. Effects of borehole stress concentrations on dipole anisotropy measurements. Geophysics 63 (1), 11–17. https://doi.org/10.1190/1.1444303.

Winkler, K.W., McGowan, L., 2004. Nonlinear acoustoelastic constants of dry and saturated rocks. J. Geophys. Res. Solid Earth 109 (B10), B10204. https://doi.org/10.1029/2004JB003262.

Yang, D.H., Zhang, Z.J., 2000. Effects of the Biot and the squirt-flow coupling interaction on anisotropic elastic waves. Chin. Sci. Bull. 45, 2130–2138. https://doi.org/10.1007/BF02886316.

Yang, D.H., Zhang, Z.J., 2002. Poroelastic wave equation including the Biot/squirt mechanism and the solid/fluid coupling anisotropy. Wave Motion 35, 223–245. https://doi.org/10.1016/S0165-2125(01)00106-8.

Yang, J.Y., Zhang, F.C., Sun, Z.T., Zheng, X.X., 2023. Nonlinear constitutive relation in acoustoelastic-orthotropic media and its wide azimuth seismic reflection coefficient characteristics for in-situ stress prediction. J. Appl. Geophys. 204, 105063. https://doi.org/10.1016/j.jappgeo.2023.105063.

Yang, L., Yang, D.H., Nie, J.X., 2014. Wave dispersion and attenuation in viscoelastic isotropic media containing multiphase flow and its application. Sci. China Phys. Mech. 57, 1068–1077. https://doi.org/10.1007/s11433-014-5435-z.

Yang, X.T., Bryan, J., Okubo, K., Jiang, C.X., Timothy Clements, T., Denolle, M.A., 2022. Optimal stacking of noise cross-correlation functions. Geophys. J. Int. 232 (3), 1600–1618. https://doi.org/10.1093/gji/ggac410.

Yin, X.Y., Zong, Z.Y., Wu, G.C., 2015. Research on seismic fluid identification driven by rock physics. Sci. China. Earth. Science 58, 159–171. https://doi.org/10.1007/s11430-014-4992-3.

Zhang, B.Y., Yang, D.H., Cheng, Y.F., Zhang, Y.Y., 2019. A unified poroviscoelastic model with mesoscopic and microscopic heterogeneities. Sci. Bull. 64 (17), 1246–1254. https://doi.org/10.1016/J.SCIB.2019.05.027.

Zoeppritz, K., 1919. Über Erdbebenwellen VII. VIIb. Über Reflexion und Durchgang seismischer Wellen durch Unstetigkeitsflächen. Nachrichten von der Gesellschaft der Wissenschaften zu Göttingen. Mathematisch-Physikalische Klasse 1, 66–84 (in German). https://eudml.org/doc/59042.

Zong, Z.Y., Yin, X.Y., Wu, G.C., 2013. Direct inversion for a fluid factor and its application in heterogeneous reservoirs. Geophys. Prospect. 61 (5), 998–1005. https://doi.org/10.1111/1365-2478.12038.